Sub-decadal Volcanic Tsunamis Due to Submarine Trapdoor Faulting at Sumisu Caldera in the Izu–Bonin Arc

Osamu Sandanbata[1,2,†], Shingo Watada[1], Kenji Satake[1], Hiroo Kanamori[3], Luis Rivera[4], and Zhongwen Zhan[3]

[1] Earthquake Research Institute, The University of Tokyo, Bunkyo, Tokyo, Japan.

[2] National Research Institute for Earth Science and Disaster Resilience, Tsukuba, Ibaraki, Japan.

[3] Seismological Laboratory, California Institute of Technology, Pasadena, CA 91125, USA.

[4] Université de Strasbourg, CNRS, ITES UMR 7063, Strasbourg F-67084, France.

Corresponding author: Osamu Sandanbata (osm3@bosai.go.jp)

† Current address: National Research Institute for Earth Science and Disaster Resilience, Tsukuba, Ibaraki, Japan.

Key Points:

- Large tsunamis are generated by moderate-sized volcanic earthquakes at a submarine caldera.
- Tsunami and seismic data indicate that abrupt uplift of the submarine caldera by trapdoor faulting causes large tsunamis.
- Continuous magma supply into the submarine caldera induces submarine trapdoor faulting on a decadal timescale.

Abstract

The main cause of tsunamis is large subduction zone earthquakes with seismic magnitudes M_w > 7, but submarine volcanic processes can also generate tsunamis. At the submarine Sumisu caldera in the Izu–Bonin arc, moderate-sized earthquakes with M_w < 6 occur almost once a decade and cause meter-scale tsunamis. The source mechanism of the volcanic earthquakes is poorly understood. Here we use tsunami and seismic data for the recent 2015 event to show that abrupt uplift of the submarine caldera, with a large brittle rupture of the ring fault system due to overpressure in its magma reservoir, caused the earthquake and tsunami. This submarine trapdoor faulting mechanism can efficiently generate tsunamis due to large vertical seafloor displacements, but it inefficiently radiates long-period seismic waves. Similar seismic radiation patterns and tsunami waveforms due to repeated earthquakes indicate that continuous magma supply into the caldera induces quasi-regular trapdoor faulting. This mechanism of tsunami generation by submarine trapdoor faulting underscores the need to monitor submarine calderas for robust assessment of tsunami hazards.

Plain Language Summary

Tsunamis are mainly caused by large submarine earthquakes, but submarine volcanic processes can also trigger tsunamis. Disproportionately large tsunami waves have been generated every decade by moderate-sized volcanic earthquakes at a submarine volcano with a caldera structure, called Sumisu caldera, in the Izu–Bonin arc, south of Japan. Despite the moderate earthquake size, the maximum wave heights of the tsunamis were about a meter, and their source mechanism has been controversial. In this study, we used tsunami and seismic data from a recent earthquake to show that the submarine caldera abruptly uplifts due to brittle rupture of its intra-

caldera fault system driven by overpressure of magma accumulating in its underlying magma reservoir and generates large tsunamis almost once a decade. The atypical source mechanism for tsunami generation suggests that it is important to monitor active submarine calderas for assessing tsunami hazards.

1 Introduction

Large earthquakes in subduction zones with seismic moment magnitudes $M_w > 7$ are the main causes of tsunamis, but other submarine geophysical processes, such as volcanism or landslides, can also trigger tsunamis (Kanamori, 1972; Paris, 2015; Satake, 2015; Ward, 2001). Because the latter generally do not cause significant seismic ground motion, the difficulty in forecasting tsunamis results in increased tsunami risk to coastal societies (Grilli et al., 2019; Hunt et al., 2021; Tappin et al., 1999; Walter et al., 2019). Unusual tsunamis have been reported for earthquakes generated at Sumisu caldera (also known as Smith caldera), which is a submarine volcano with an 8 km × 10 km caldera structure in the Izu–Bonin arc (Figure 1) (Shukuno et al., 2006; Tani et al., 2008). At the caldera, volcanic earthquakes with moderate seismic magnitudes (M_w 5.4–5.7) have occurred quasi-regularly in 1984, 1996, 2006, 2015, and 2018 (Figure 1b; Table S1), which are known as Torishima earthquakes (Fukao et al., 2018; Kanamori et al., 1993; Satake & Kanamori, 1991). The earthquake on 2 May 2015 (M_w 5.7) caused a disproportionally large tsunami with a maximum wave height of 1 m on Hachijojima Island, located 180 km north of the caldera (Figure 1c), although no ground shaking was felt on the island. The other four earthquakes also caused relatively large tsunamis with similar waveforms at many tide gauge stations (Figures 1d–e and S1). The five earthquakes were seismologically similar to each other, and all had a moment tensor with a large compensated-

linear-vector-dipole (CLVD) component and a dominant nearly vertical tension axis (Figure 1b), which is often called a vertical-T CLVD earthquake (Shuler, Ekström, et al., 2013; Shuler, Nettles, et al., 2013).

Since the 1984 earthquake, various models have been proposed for this atypical earthquake mechanism and tsunami generation. These include dip slip on a curved ring fault system of a caldera (Ekström, 1994), vertical opening of a shallow horizontal crack (Fukao et al., 2018), and volume change due to fluid injection at shallow depth (Kanamori et al., 1993; Satake & Kanamori, 1991). However, different interpretations can explain the moment tensors (Shuler, Ekström, et al., 2013), and no consensus on the earthquake mechanism has yet been reached, because of the inaccessibility of the submarine caldera. For the 2015 earthquake, the tsunami was recorded by high-quality ocean bottom pressure (OBP) gauges of a temporary array and recently deployed tsunami observation networks to the south of Japan (Figure 1a). The obtained tsunami waveform and regional seismic data provide an opportunity to determine the mechanisms responsible for these anomalous volcanic earthquakes.

The objective of this study is to determine the source mechanism of the volcanic earthquakes at Sumisu caldera. We initially conduct a preliminary analysis using only the tsunami waveform data to estimate the sea-surface disturbance due to the coseismic seafloor deformation. We then combine the tsunami and long-period seismic data to develop a source model that can quantitatively explain both datasets. Based on this model, we discuss the source mechanism of the earthquakes, possible causes of the efficient tsunami excitation and their sub-decadal recurrence, and implications for the submarine volcanism of Sumisu caldera.

89 **2 Data**

90 2.1 Tsunami data

91 We use tsunami data recorded by 24 OBP gauges (Figure 1a) of the array off Aogashima
92 Island, the Dense Oceanfloor Network system for Earthquakes and Tsunamis (DONET) system,
93 the Deep Sea Floor Observatory (DSFO) off Muroto Cape, and the Deep-ocean Assessment and
94 Reporting of Tsunamis (DART) system. We manually check the data quality (i.e., data gaps,
95 spikes, or repeated values) near the arrival times of the tsunami signals and remove tidal trends
96 by fitting polynomial functions. Following Sandanbata, Watada, et al. (2021), we apply a two-
97 pass second-order low-pass Butterworth filter to the tsunami waveforms. The cut-off frequencies
98 are 0.0125, 0.0083, 0.0083, and 0.00667 Hz for stations from the array, DONET, DSFO, and
99 DART, respectively, depending on the maximum depth along a source–station path.

100

101 2.2 Long-period seismic data

102 We use seismic data recorded by the BH channel (three components) of 36 regional
103 stations (epicentral distance < 30°) of the F-net and Global Seismograph Network (GSN). The
104 seismic stations are listed in Table S2. We remove the instrument response from the observed
105 seismograms to obtain the displacement records and apply a one-pass fourth-order band-pass
106 Butterworth filter with corner frequencies of 0.004 and 0.0167 Hz (band-pass period = 60–250 s)
107 using the W-phase package (Duputel et al., 2012; Hayes et al., 2009; Kanamori & Rivera, 2008).

108

3 Preliminary analysis: Estimation of the initial sea-surface displacement

As a preliminary step for the source modeling of the 2015 earthquake, we estimate the initial sea-surface displacement caused by the earthquake using a tsunami waveform inversion method. To compute synthetic tsunami waveforms, we first assume 113 unit sources of sea-surface displacement at 2-km intervals in a source area of 32 km × 32 km around Sumisu caldera (Figure S2). Each unit source has a cosine-tapered shape (Hossen et al., 2015):

$$\eta^k(x,y) = 0.25 \times \left[1.0 + \cos\frac{\pi(x-x^k)}{L}\right] \times \left[1.0 + \cos\frac{\pi(y-y^k)}{L}\right], \quad (|x - x^k|, |y - y^k| \le L) \tag{1}$$

where (x^k, y^k) is the central location in kilometers of the kth unit source ($k = 1, 2, \ldots, K$; here K = 113) with a source size of $2L$ (i.e., 4.0 km). The rise time for each unit source is 10 s, given that the earthquake source duration is 10 s as estimated by our moment tensor analysis (Text S1; Table S3).

We then simulate tsunami propagation over the ocean from the assumed unit sources. To compute a tsunami waveform with relatively long-period components at the most distant station 52404 (located ~1,400 km from the epicenter), we use a phase correction method developed for long-period tsunamis (Ho et al., 2017). In this method, we first solve the linear long-wave equations with the JAGURS code (Baba et al., 2015) and then correct the phase spectra to incorporate the effects of the dispersion, the compressibility and the density stratification of seawater, and the elasticity of the Earth. On the other hand, tsunami waveforms at the other stations at shorter distances are dominated by shorter-period waves, which makes it inadequate to use the linear long-wave equations. Hence, we use a different phase correction method that was developed for short-period tsunamis (Sandanbata, Watada, et al., 2021). In this method, we solve

129 the linear Boussinesq equations (approximately including dispersion) by the JAGURS code and
130 corrected the phase spectra to incorporate the accurate dispersion, the effects of seawater
131 compressibility and density stratification, and the Earth's elasticity. The latter phase correction
132 method incorporates variations in ray paths of highly dispersive short-period waves and enables
133 us to compute short-period waveforms more accurately. In both cases, the computational time-
134 step interval is 0.25 s. We use high-resolution bathymetric data (10 arcsec, ~300 m, grid spacing)
135 processed from M7000 Digital Bathymetric Chart (M7022) for the area near Sumisu caldera and
136 Aogashima Island, whereas we use JTOPO30 and GEBCO_2014 (30 arcsec grid spacing) for the
137 other regions. When the tsunami wavelength is comparable to or shorter than the water depth, the
138 bottom pressure change becomes smaller and smoother than that just beneath the sea surface
139 which is equivalent to the static water pressure of the wave height. To include this pressure
140 reduction effect, we apply a spatial low-pass filter, often referred to as the Kajiura filter (Kajiura,
141 1963), to the wave-height field output for every 5.0 s and obtain the OBP change at the stations
142 (Chikasada, 2019). We also apply the low-pass Butterworth filter to the time series of the OBP
143 change as used for the OBP data. Hereafter, the tsunami waveforms are OBP waveforms (in the
144 [cm H_2O] scale).

145 After computing the synthetic tsunami waveforms $g_j^k(t)$ from the *k*th unit source to the
146 *j*th station ($j = 1, 2, \dots, J$; here J = 24), we solve a linear inverse problem to estimate the initial
147 sea-surface displacement. Because the wave amplitudes of the near-field data (a few centimeters)
148 are much larger than those of the regional-field data (a few millimeters), we normalize the
149 observed and synthetic waveforms at the *j*th station by the weight w_j, following the method of
150 Ho et al. (2017). The weight is the inverse root-mean-square (RMS) value of the observed
151 waveform at each station:

$$\frac{1}{w_j} = \sqrt{\frac{\sum_{l=0}^{\gamma_j}\{d_j(t_l)\}^2}{\gamma_j}}, \tag{2}$$

where $d_j(t_l)$ is the tsunami waveform data for the *j*th station and γ_j is the number of data points used for the analysis. Using the normalized observed and synthetic waveform data, we solve the following observation equation with the damped least-squares method (pp. 695–699 in Aki & Richards, 1980):

$$\begin{bmatrix}\overline{\boldsymbol{d}}\\ \mathbf{0}\end{bmatrix} = \begin{bmatrix}\overline{\boldsymbol{g}}\\ \alpha\boldsymbol{I}\end{bmatrix}\boldsymbol{m}, \tag{3}$$

where $\overline{\boldsymbol{d}} = [w_1 d_1(t) \quad \cdots \quad w_J d_J(t)]^T$ and $\overline{\boldsymbol{g}} = \begin{bmatrix} w_1 g_1^1(t) & \cdots & w_1 g_1^K(t) \\ \vdots & \ddots & \vdots \\ w_J g_J^1(t) & \cdots & w_J g_J^K(t) \end{bmatrix}$ are the column vector of the observed waveform data $d_j(t)$ and the matrix of the synthetic waveform data $g_j^k(t)$ weighted by w_j at the *j*th station (Equation 2), respectively, and $\boldsymbol{m} = [m^1 \quad \cdots \quad m^K]^T$ is an unknown column vector of the amplitude factors to be multiplied by the *k*th unit source, $\boldsymbol{I}$ is the identity matrix, and α is the damping parameter used to obtain a smooth model. We assume α = 2.0 to achieve an appropriate trade-off between the waveform fit and the smoothness of the solution (Figure S3).

Thus, we obtain an initial sea-surface displacement model, composed of a sea-surface uplift of about 1 m over the caldera floor, with its uplift peak shifted northeastward relative to the caldera center, and smaller subsidence outside of the caldera rim mainly on the northeastern side (Figure 2a). This model reproduces the tsunami waveform data (Figure S4). To examine the robustness of the exterior subsidence, we estimate the initial sea-surface uplift model, without subsidence, by imposing a non-negative condition ($\boldsymbol{m} \geq \mathbf{0}$) when solving Equation 3. The

obtained uplift model, containing only a larger northeastern uplift, cannot reproduce the tsunami first motions with initial downswing signals of the relatively near-field stations in the northeastern direction (A01–10; Figure 2b). This result suggests that, during the earthquake, the exterior of the caldera subsided at least on its northeastern side. Note that a previous study (Fukao et al., 2018) assumed a symmetrical caldera floor uplift model surrounded by peripheral subsidence to explain the tsunami waveforms at the array off Aogashima Island, but Sandanbata, Watada, et al. (2021) demonstrated that the model of Fukao et al. (2018) does not explain the tsunami arrival times at the stations of DONET, DSFO and DART. Our tsunami waveform inversion using all the OBP data with wider azimuthal coverage suggests that the uplift and the subsidence were localized on the northeastern side of the caldera.

4 Source modeling of the 2015 earthquake: methodology

4.1 Hypothetical earthquake source system

We next explore the source model of the 2015 earthquake by combining analyses of the tsunami and long-period seismic data. From the deformation pattern determined in the preliminary analysis (Section 3), we assume an earthquake source system composed of dip slip of an elliptical fault system and vertical deformation of a shallow horizontal crack beneath Sumisu caldera (Figure 3a). This assumption of the fault-crack composite system is inspired by previous caldera modeling studies that discussed interactive systems beneath calderas between a circular or elliptical fault, called *ring fault*, and a sill-like magma reservoir (e.g., Yun, 2007; Bathke et al., 2015; Liu et al., 2019; Galetto et al., 2019; Zheng et al., 2022). Most calderas are known to have pre-existing ring fault systems formed during caldera collapse in the past (e.g.,

Cole et al., 2005; Roche et al., 2000), where faulting events called *ring-faulting* sometimes take place in response to pressure change in an underlying magma reservoir (e.g., Ekström, 1994; Shuler, Ekström, et al., 2013; Contreras-Arratia & Neuberg, 2019; Sandanbata, Kanamori, et al., 2021). For example, at the subaerial caldera of Sierra Negra in the Galapagos Islands, seismic events characterized by vertical-T CLVD moment tensors occurred in such a sub-caldera interactive system, and caused large asymmetric uplifts of the caldera floor (e.g., Amelung et al., 2000; Chadwick et al., 2006; Jónsson, 2009) like what was estimated for the 2015 earthquake at Sumisu caldera in Section 3. Some previous studies (e.g., Yun, 2007; Zheng et al., 2022) explained geodetic data at Sierra Negra caldera by proposing source models that combine ring-faulting and deformation of its underlying horizontal crack; this inferred mechanism is especially referred to as *trapdoor faulting*. Given such successful examples of caldera modeling, the fault-crack composite system can be a good candidate for the earthquake source at Sumisu caldera. Caldera-floor cones, some of which were identified as young lava domes (Tani et al., 2008), are located along a line forming an elliptical shape on the floor of Sumisu caldera (Figure 1b); this also indicates that a ring fault system is connected to a shallow reservoir filled with magma (Cole et al., 2005).

4.2 Tsunami waveform inversion for fault-crack composite source models

We again use a tsunami waveform inversion method with the OBP data but this time to directly determine motions of the fault-crack composite system (i.e., dip-slip dislocations of the ring fault and tensile dislocations of the horizontal crack). The inversion procedure is as follows.

4.2.1 Source structure

213 To model the fault-crack composite system beneath Sumisu caldera, we assume reverse
214 slip for an inward-dipping ring fault and vertical deformation (opening or closing) for a
215 horizontal crack (Figures 3a). We consider reverse slip of the inward-dipping ring fault, because
216 vertical-T CLVD earthquakes accompanying a caldera floor uplift are expected for the
217 combination of the slip and dip directions of the ring-faulting (see Figure 9 in Shuler, Ekström, et
218 al., 2013, or Figure 1 in Sandanbata, Kanamori, et al., 2021). The ring fault is elliptical with its
219 center at (140.0454°E, 31.4816°N) and its major axis oriented N70°E, and its horizontal size is
220 3.0 km × 2.7 km on the seafloor. The ring fault may not be a full ring; the arc length is varied as
221 1/3, 2/3 and 1 (full ring), but the midpoint is fixed to the northeastern corner of the caldera
222 (Figures 3b–d). The ring fault extends with a uniform inward dip angle from the seafloor to the
223 edge of the elliptical horizontal crack. We try tens of source structures with three variable
224 geometric parameters: (a) the depth of the horizontal crack (3 or 6 km); (b) the dip angle of the
225 ring fault (70–90°); and (c) the arc length of the ring fault (1/3, 2/3, or full ring).

226 We discretize the source structures into triangular source elements. The ring fault is
227 divided into triangular elements with an arc angle of 22.5° along the circumference and 1 km
228 along the depth, and a trapezoid composed of two neighboring triangular elements with the same
229 dip and strike angles is regarded as a sub-fault. The horizontal crack is discretized by triangular
230 elements using the DistMesh code (Persson & Strang, 2004), and each element is regarded as a
231 sub-crack. Assuming the geometry of sub-faults and sub-cracks, we will determine dislocation
232 amounts of reverse slip at each sub-fault and opening (or closing) at each sub-crack, which are
233 denoted by $\boldsymbol{s} = [s_1 \quad \cdots \quad s_{N_s}]^T$ and $\boldsymbol{\delta} = [\delta_1 \quad \cdots \quad \delta_{N_\delta}]^T$, respectively. Since the dislocations of
234 the ring fault and the horizontal crack should be consistent at their contacts, we impose a
235 kinematic condition that links the vertical component of the sub-fault slip at the ring fault bottom

to the sub-crack opening/closing at the crack edge adjacent to the sub-fault. The kinematic condition can be written as:

$$s_p \sin \Delta_p = \delta_q, \tag{4}$$

where Δ_p is the dip angle of the *p*th sub-fault to which the *q*th sub-crack is adjacent.

4.2.2 Computation of the tsunami Green's functions

We then compute synthetic tsunami waveforms, or Green's functions G_{ij}, relating the dislocation (i.e., reverse slip of the sub-fault and vertical opening of the sub-crack) of the *i*th source element ($i = 1, 2, \ldots, I$; I depends on the source structures) to the tsunami waveform at the *j*th station. For this purpose, we reuse the synthetic tsunami waveforms g_j^k from unit sources of sea surface displacement η^k, which were computed in Section 3. By reusing g_j^k, we do not have to simulate tsunami propagation over the ocean as done in Section 3, which significantly reduces the computational cost and helps us to efficiently assess the inversions for tens of source structures, each of which consists of $I > 50$ source elements. The computation of G_{ij} is performed with the following three steps.

First, we calculate the vertical seafloor displacements from 1 m reverse slips of sub-faults and 1 m opening of sub-cracks with the triangular dislocation (TD) method (Nikkhoo & Walter, 2015) assuming a Poisson's ratio of 0.25 and a flat seafloor, and we convert the seafloor displacements into the vertical *sea-surface* displacements by applying the Kajiura filter (Kajiura, 1963) assuming a water depth of 800 m; this filtering process is required because the resultant vertical sea-surface displacement becomes smaller and smoother than that at the seafloor when the horizontal scale of the seafloor displacement is comparable to or smaller than the water depth

(e.g., Saito & Furumura, 2013). We thus denote the vertical sea-surface displacement from the *i*th source element $h_i(x, y)$.

Second, the computed sea-surface displacement $h_i(x, y)$ is approximated by a linear combination of the unit sources of sea-surface displacement $\eta^k(x, y)$ (Equation 1; Figure S2):

$$h_i(x, y) \approx \sum_{k=1}^{K} m_i^k \eta^k(x, y), \tag{5}$$

where the amplitude factors m_i^k are obtained by a least-squares method.

Third, we obtain Green's functions relating the *i*th source element to the *j*th station by superimposing the synthetic tsunami waveforms from the *k*th unit sources $g_j^k(t)$ multiplied by the amplitude factors m_i^k, as follows:

$$G_{ij}(t) = \sum_{k=1}^{K} m_i^k g_j^k(t). \tag{6}$$

4.2.3 Inverse problem

Finally, we solve the observation equation with the kinematic condition (Equation 4) by the damped least-squares method:

$$\begin{bmatrix} \bar{\boldsymbol{d}} \\ \boldsymbol{0} \\ \boldsymbol{0} \end{bmatrix} = \begin{bmatrix} \bar{\boldsymbol{G}} \\ \boldsymbol{K} \\ \beta \boldsymbol{I} \end{bmatrix} \begin{bmatrix} \boldsymbol{s} \\ \boldsymbol{\delta} \end{bmatrix}, \tag{7}$$

where $\bar{\boldsymbol{d}}$ is the column vector of the observed tsunami waveforms d_j normalized by w_j at the *j*th station (Equation 2), and $\bar{\boldsymbol{G}} = \begin{bmatrix} w_1 G_{11}(t) & \cdots & w_1 G_{I1}(t) \\ \vdots & \ddots & \vdots \\ w_J G_{1J} & \cdots & w_J G_{IJ}(t) \end{bmatrix}$ is the matrix of the Green's functions G_{ij} normalized by w_j. $\boldsymbol{s}$ is an unknown column vector of reverse slip amounts for sub-faults of the ring fault, for which we impose the non-zero condition ($\boldsymbol{s} \geq \boldsymbol{0}$), and $\boldsymbol{\delta}$ is an unknown column vector of opening amounts for sub-cracks of the horizontal crack, for which we allow either

positive (opening) or negative (closing) values. The linear equation of $\boldsymbol{K}\begin{bmatrix}\boldsymbol{S}\\ \boldsymbol{\delta}\end{bmatrix} = \boldsymbol{0}$ represents the kinematic condition of Equation 4. β is the damping parameter for smoothing, which we set at 0.3, by balancing the waveform fit and the smoothness of the motion (Figure S5). The inversion time windows include several wave crests and troughs. Thus, we determine motions of the fault-crack composite systems and obtain source models based on the tsunami data.

To evaluate the model performance, we calculate the normalized root-mean-square (NRMS) misfit of the tsunami waveforms, which we term the tsunami waveform misfit:

$$\rho^t = \sqrt{\sum_j \left\| \boldsymbol{c}_j^t - \boldsymbol{d}_j^t \right\|^2 / \sum_j \left\| \boldsymbol{c}_j^t \right\|^2}, \tag{8}$$

where $\boldsymbol{c}_j^t$ and $\boldsymbol{d}_j^t$ are the column vectors of the synthetic and observed tsunami waveforms of the model in inversion time window at the *j*th station, respectively. $\| \ \|$ denotes the L2 norm.

4.3 Computation of the long-period seismic waveforms

For validation of the fault-crack composite source model inverted from the tsunami data, we compute long-period seismic waveforms for the model and compare them with the long-period seismic data. Because the wavelength of seismic data we use is much longer than the size of the caldera, the seismic source can be modeled by a point-source moment tensor. The total moment tensor $\boldsymbol{M}$ of the source model is calculated as:

$$\boldsymbol{M} = \boldsymbol{M}_{RF} + \boldsymbol{M}_{HC} = \sum \boldsymbol{m}_{RF}^p + \sum \boldsymbol{m}_{HC}^q, \tag{9}$$

where $\boldsymbol{M}_{RF}$ and $\boldsymbol{M}_{HC}$ are the moment tensors of the ring fault and horizontal crack, respectively, and $\boldsymbol{m}_{RF}^p$ and $\boldsymbol{m}_{HC}^q$ are the moment tensors of the *p*th sub-fault slip and the *q*th sub-crack opening

or closure, respectively (Figure S6a). The coordinate system is (r, θ, ϕ) for [up, south, east]. $\boldsymbol{m}_{RF}^{p}$ is computed from the reverse slip amount and strike, dip, and rake (90°) angles of the pth sub-fault (Box 4.4 in Aki & Richards, 1980). The seismic moment is computed as $\mu s_p A_p$, where s_p and A_p are the reverse slip amount and area of the pth sub-fault, and μ is the rigidity, or Lamé's constant. $\boldsymbol{m}_{HC}^{q}$ is calculated as:

$$\boldsymbol{m}_{HC}^{q} = \begin{bmatrix} M_{rr} & M_{\theta r} & M_{\phi r} \\ M_{r\theta} & M_{\theta\theta} & M_{\phi\theta} \\ M_{r\phi} & M_{\theta\phi} & M_{\phi\phi} \end{bmatrix} = \delta_q \times A_q \times \begin{bmatrix} \lambda + 2\mu & 0 & 0 \\ 0 & \lambda & 0 \\ 0 & 0 & \lambda \end{bmatrix}, \quad (10)$$

where δ_q and A_q are the opening amount and area of the qth sub-crack, respectively (Kawakatsu & Yamamoto, 2015). Lamé's constants λ and μ are assumed to be 29.90 and 31.85 GPa, respectively, based on the P- and S-wave velocities (V_p = 6.0 km/s and V_s = 3.5 km/s) and the density ($\rho_0 = 2.6 \times 10^3$ kg/m^3) in the shallowest layer of the Earth model (Figure S6b). The scalar seismic moment of the moment tensor is $M_0 = \sqrt{\Sigma_{ij} M_{ij} M_{ij}/2}$ (pp. 166–167 in Dahlen & Tromp, 1998; Silver & Jordan, 1982), and the moment magnitude is $M_w = \frac{2}{3}(\log_{10} M_0 - 9.10)$, with M_0 in the [N m] scale (Hanks & Kanamori, 1979; Kanamori, 1977).

By assuming the moment tensor (Equation 9), we compute the long-period (60–250 s) seismic waveforms with the W-phase package (Duputel et al., 2012; Hayes et al., 2009; Kanamori & Rivera, 2008). We compute the Green's functions of the seismic waveforms for the one-dimensional crustal velocity model for Japan (Figure S6b) using the wavenumber integration method (Herrmann, 2013). We fix the centroid location at a depth of 1.5 km below the seafloor in the center of Sumisu caldera (140.053°E, 31.485°N). The half duration of the source time function and the centroid time shift relative to the origin time reported by the Global CMT (GCMT) catalogue (Ekström et al., 2012; Table S1) are assumed to be 5 s, based on our moment

tensor analysis (Table S3). We apply the same filter as for the seismic data (see Section 2.2) to the synthetic waveforms.

To evaluate the model performance, we calculate the NRMS misfit of the long-period seismic waveforms, which we term the seismic waveform misfit:

$$\rho^s = \sqrt{\sum_j \left\| \boldsymbol{c}_j^s - \boldsymbol{d}_j^s \right\|^2 / \sum_j \left\| \boldsymbol{c}_j^s \right\|^2}, \quad (11)$$

where $\boldsymbol{c}_j^s$ and $\boldsymbol{d}_j^s$ are the column vectors of the synthetic and observed seismic records at the *j*th channels, respectively. We set the time window to include the P, S, and surface waves.

5 Source modeling of the 2015 earthquake: Results

By the tsunami waveform inversion, we obtain tens of fault-crack composite source models for the 2015 earthquake with different combinations of the three geometric source parameters (i.e., the depth of the horizontal crack, the dip angle and arc length of the ring fault). As an example, Figure 4a shows the result when the horizontal crack is at a 3 km depth and the ring fault has a dip angle of 85.0° and a 2/3-ring arc length. This model shows that the ring fault has nonzero slips at all depths that are consistent with the horizontal crack motions at the bottom (Figure 4b). The nonzero slips at all the depths are obtained for most models with the horizontal crack at a depth of 3 km. By contrast, if we assume that the horizontal crack is at a depth of 6 km, the ring fault has a zone with zero slip in the middle depth of the ring fault (Figure S7), which we consider unrealistic for the fault system. Hence, we suggest that the horizontal crack is at a shallower depth and hereafter show models with a horizontal crack at the depth of 3 km.

Figure 5 shows the tsunami NRMS misfit for the models with the crack at 3-km depth. The misfit varies only slightly as a function of the dip angle and the arc length of the ring fault. Figure 6 shows that the source model with a 2/3-ring arc length (shown in Figure 4a) reproduces the observed tsunami data well. Similarly, models with a full or 1/3-ring arc length yield good waveform fits (Figures S8 and S9). These indicate that the tsunami waveform data provide little constraint on the ring-fault parameters. However, we emphasize that, irrespective of the assumed ring-fault arc length (2/3, full, or 1/3-ring), the obtained source models are expected to similarly cause larger sea-surface uplifts over the northeastern part of the caldera but much smaller over the southwestern part (see Figures 6a, S8b, and S9b). This implies that the ring-faulting occurred mainly around the northeastern side but was minor (if any) on the southwestern side.

To further constrain the model, we use the long-period seismic data. In contrast to the tsunami data, the seismic data are useful to constrain the ring-fault parameters. In Figure 5, we plot the seismic NRMS misfit as a function of the dip angle and the arc length of the ring fault. First, the seismic waveform misfit strongly depends on the ring-fault dip angle. Figure 7 compares fault-crack motions, moment tensors, and synthetic seismograms of three models with different dip angles (but similarly with a 2/3-ring arc length), showing that the amplitudes of seismic waveforms are significantly different despite similar slip amounts and M_w determined by the tsunami waveform inversion. This is because the ring-faulting at such a shallow depth becomes less efficient in radiating long-period seismic waves as the dip angle becomes closer to the vertical (Sandanbata, Kanamori, et al., 2021). From the seismic NRMS misfits (Figure 5), we determine optimal dip angles to be 85.0°, 85.5°, and 83.5 for 2/3, full, and 1/3-ring arc lengths, respectively. Note that if we assume a smaller rigidity for the shallow source depth, the optimal dip angles become smaller (see Text S2).

Among the three models with the optimal dip angles, the 2/3-ring arc-length model yields the smallest seismic NRMS misfit of 0.425 (Figure 5; 0.465 and 0.480, for the full and 1/3-ring arc lengths, respectively); this model is shown in Figure 4a. Figure 8 shows the moment tensors and synthetic seismograms for the 2/3-ring arc-length model, which overall explain the observed seismic waveforms. For comparison, we show in Figures S10 and S11 the cases for the full and 1/3-ring arc-length models with the optimal dip angles. The preference of the 2/3-ring arc-length model over the other two models can be seen in the better phase fits of the horizontal components at some stations (e.g., BHE channel of KZS, YMZ, and TYS, and BHN channel of AMM in Figures 8d, S10d, and S11d). As shown in Sandanbata, Kanamori, et al. (2021), the seismic radiation pattern of the ring-faulting is sensitive to the ring-fault arc length, and the side on which the ring fault is placed, because of the geometrical cancelation of double-couple components of the moment tensor (see Figure 2 of Sandanbata, Kanamori, et al., 2021, for example). This property causes differences in seismic waveforms of the three arc-length models, which helps us to select the 2/3-ring arc-length model as the most preferable model.

In summary, based on the tsunami and seismic analyses above, we consider the model shown in Figure 4a as our best-fit source model for the 2015 earthquake. This model has a horizontal crack at the depth of 3 km and a ring fault with an inward dip angle of 85° along a 2/3-ring arc length, on both of which large dislocations are determined. The ring fault has a maximum reverse slip of 6.8 m on its northeastern side. The vertical opening of the horizontal crack is a maximum of 2.7 m on its eastern side, whereas its closure is 5.0 m on its southwestern side. The net volume increase of the horizontal crack calculated with the model is 1.26×10^7 m^3. Figure 4c shows the subsurface displacements due to the combination of the ring-faulting and the crack deformation, calculated by the TD method, which represents the asymmetric motion of the

375 caldera block. The maximum upward displacement is about 4 m on the inner side of the
376 northeastern ring fault, while the maximum downward displacement is about 2 m on the
377 southwestern upper wall of the horizontal crack.

378 The vertical sea-surface displacement caused by the best-fit source model (Figure 6a)
379 presents uplift twice as large as and more localized than our preliminary analysis estimated
380 (Figure 2a), but explains equally well the tsunami waveform data at all the OBP gauges (Figure
381 6b). Note that in the preliminary analysis, the main uplift was estimated in a relatively broader
382 area (Figure 2a) because of no constraint from the source structure, possibly leading to the
383 underestimation of the amplitude.

384 Figure 9 compares the contributions of the ring fault and the horizontal crack to tsunamis
385 at representative stations. Tsunami waveforms from the two parts are more different at shorter
386 distances (see A01–A04), indicating the importance of near-field tsunami observations to
387 distinguish the two sources. We note that if we perform the tsunami waveform inversion by
388 assuming only either the ring fault or the horizontal crack, the waveform fit clearly deteriorates
389 (Figures S12 and S13), demonstrating that the fault-crack composite source model is an
390 appropriate model for the earthquake.

391 The moment tensor of the best-fit source model (Figure 8a) with a large isotropic
392 component consists of the ring fault (Figure 8b) and the horizontal crack (Figure 8c)
393 components. This model explains well the long-period seismic data at most stations, as shown in
394 Figure 8d. Although slight waveform discrepancies are seen in several records (e.g., BHE
395 channel of KZS, YMZ, and TYS, and BHN channel of AMM), they can be substantially reduced
396 by performing the source modeling with slight modifications of dip angles in parts of the ring
397 fault (see Text S3, Figures S14 and S15).

398 To consider contributions to long-period seismic waves from each of source parts, we
399 show in Figure 10 long-period seismograms computed for the three partial moment tensors from
400 our best-fit source model: (a) the ring fault only ($\boldsymbol{M_{RF}}$: M_w 6.11); (b) the horizontal crack only
401 ($\boldsymbol{M_{HC}}$: M_w 5.91); and (c) the ring fault only, but without $M_{r\theta}$ and $M_{r\phi}$ (i.e., M_{rr}, $M_{\theta\theta}$, $M_{\phi\phi}$, and
402 $M_{\theta\phi}$ of $\boldsymbol{M_{RF}}$: M_w 5.71). The seismic magnitude of $\boldsymbol{M_{HC}}$ is comparable to that of $\boldsymbol{M_{RF}}$, but the
403 seismic amplitudes from $\boldsymbol{M_{HC}}$ are much smaller than those from $\boldsymbol{M_{RF}}$ (compare Figures 10a and
404 10b). Additionally, synthetic seismograms from $\boldsymbol{M_{RF}}$ change little even after excluding the two
405 moment tensor elements ($M_{r\theta}$ and $M_{r\phi}$; compare Figures 10a and 10c), showing the very small
406 contribution by the two elements. These highlight the very small long-period seismic excitations
407 from the horizontal crack and the two elements ($M_{r\theta}$ and $M_{r\phi}$) of the ring fault that occur at
408 shallow depths near the free-traction seafloor surface (pp. 180–183 of Dahlen & Tromp, 1998;
409 Fukao et al., 2018; Sandanbata, Kanamori, et al., 2021). Thus, despite the seismic magnitude M_w
410 6.16 of $\boldsymbol{M_{HC} + M_{RF}}$ (a seismic moment $M_0 = 2.16 \times 10^{18}$ Nm; Figure 8a), only the limited part
411 of the ring-faulting $\boldsymbol{M_{RF}}$, excluding the two elements, that corresponds to M_w 5.71 ($M_0 = 0.46 \times$
412 10^{18} Nm; equivalent to 22% of the total seismic moment; Figure 10c), contributes the long-
413 period seismic radiation of the fault-crack composite source model. We note that the four
414 moment tensor elements of the ring fault contributing to the seismic waves constitute a vertical-T
415 CLVD-type moment tensor (Figure 10c), which agrees with the solution reported in the GCMT
416 catalog (Ekström et al., 2012) (Figure 1b).

417

6 Discussion

6.1 Submarine trapdoor faulting at Sumisu caldera

We have shown that the fault-crack composite source model (Figure 4a) explains quantitatively both the tsunami and long-period seismic data of the 2015 earthquake at Sumisu caldera. This source model strongly suggests the *trapdoor faulting* mechanism of the earthquake at the submarine caldera (Figure 11), like that found at the subaerial Sierra Negra caldera. As introduced briefly in Section 4.1, trapdoor faulting events have been observed geodetically several times at Sierra Negra caldera (e.g., Amelung et al., 2000; Chadwick et al., 2006; Jónsson, 2009). Based on geodetic data, many previous studies showed that the trapdoor faulting takes place in the interaction between sudden rupture of the intra-caldera ring fault and deformation of its underlying sill-like magma reservoir, and suggested that it is driven by high magma pressure within the reservoir (Amelung et al., 2000; Yun, 2007; Jónsson, 2009; Gregg et al., 2018). Recently, Zheng et al. (2022) numerically solved the mechanical interaction between the ring fault and the crack-like reservoir with magma pressure change effect, and proposed a trapdoor faulting model by fitting the geodetical data for the 2005 event of Sierra Negra caldera. Their mechanical model predicted that the trapdoor faulting caused large reverse slip of a part of an inward-dipping ring fault and asymmetric deformation of the crack-like reservoir (see Figure 2b in Zheng et al., 2022). Although our kinematic source model of the earthquake at Sumisu caldera does not consider the mechanical interaction or magma pressure change effect, the fault-crack motion patterns shown in our model (Figure 4a) are similar to those of the trapdoor faulting predicted by the mechanical model of Zheng et al.

In addition to the model similarities, trapdoor faulting events at Sierra Negra caldera share many similar features with the Sumisu caldera earthquake. First, trapdoor faulting events at

441 Sierra Negra occurred with vertical-T CLVD earthquakes of $M_w \sim 5$ (Shuler, Ekström, et al.,
442 2013; Sandanbata, Kanamori, et al., 2021) and caused meter-scale asymmetrical caldera floor
443 uplifts (Amelung et al., 2000; Chadwick et al., 2006; Jónsson, 2009). Second, the deformation
444 during a trapdoor faulting in 2005 at Sierra Negra recorded by a Global Positioning System
445 sensor near the southern intra-caldera fault occurred within 10 s (Chadwick et al., 2006; Jónsson,
446 2009), which is comparable to the rupture duration (10 s: the half duration of 5 s) estimated for
447 the earthquakes at Sumisu caldera by our moment tensor analysis (Text S1; Table S3). Third,
448 during the 2005 trapdoor faulting at Sierra Negra, the northern caldera floor, opposite from the
449 southern fault with the largest slip, subsided by a few centimeters, which was attributed to the
450 pressure drop of the inner magma reservoir (Jónsson, 2009; Zheng et al., 2022). This feature can
451 be expected similarly from our model with closure of the crack in the southwestern part of
452 Sumisu caldera.

453 Therefore, similarly to interpretations for trapdoor faulting at Sierra Negra caldera in
454 previous studies (e.g., Amelung et al., 2000; Jónsson, 2009; Zheng et al., 2022), we suggest that
455 submarine trapdoor faulting at Sumisu caldera, driven by overpressure of magma accumulating
456 in the horizontal crack, or a sill-like reservoir, caused the 2015 earthquake and tsunami (Figure
457 11). We speculate that continuous magma supply into the crack gradually increases the shear
458 stress on the pre-existing ring fault system in the interseismic process, until it reaches a critical
459 value for initiation of brittle rupture of the ring fault. Once the trapdoor faulting process initiates
460 with the ring-faulting, the top surface of the horizontal crack moves vertically upward. The
461 consequent increase in the reservoir volume depressurizes the inner magma, possibly causing the
462 closure of the southwestern part of the crack, as shown by Zheng et al. (2022). Note that Zheng
463 et al. suggested that the reservoir filled with compressible magma increases its inner volume

464 during the trapdoor faulting. Hence, our model containing a net volume increase of 1.26×10^7 m^3
465 implies that the magma beneath the caldera is compressible. Due to the volume increase and
466 depressurization of the inner magma, the trapdoor faulting may not lead to an immediate
467 submarine eruption at the caldera (Amelung et al., 2000). Our finding of submarine trapdoor
468 faulting, following the previous observations at the subaerial Sierra Negra caldera, indicates that
469 this volcanic phenomenon might be more common at calderas than previously thought.

470

471 6.2 Efficient tsunami generation mechanism

472 Trapdoor faulting produces an unusually large fault slip as compared with ordinary
473 tectonic earthquakes and can generate a large tsunami despite its moderate earthquake magnitude
474 when it occurs under water. For the 2015 earthquake (M_w 5.7 in the GCMT catalog), our best-fit
475 source model has a maximum slip of 6.8 m along the ring fault (Figure 4a). In contrast, the
476 empirical scaling law (Wells & Coppersmith, 1994) predicts that tectonic earthquakes with the
477 same moment magnitude have a maximum slip of only 0.17 m. The subaerial trapdoor faulting in
478 2005 at Sierra Negra caldera also caused a large slip of ~2 m along the intra-caldera fault, despite
479 its small seismic body-wave magnitude of 4.6 (Jónsson, 2009; Zheng et al., 2022). These
480 disproportionately large slips might be possible because the fault system connected to the
481 reservoir can effectively cause slip. Additionally, atypical source properties of trapdoor faulting
482 such as the shallow source depth, the localized stress increase due to magma overpressure, and/or
483 the fault–magma interaction during rupture, possibly contribute to large slips.

484 Submarine trapdoor faulting is efficient in generating tsunamis, even for the relatively
485 low seismic magnitude of the earthquakes, due to its shallow and complex source structure.

Firstly, trapdoor faulting occurring above a shallow magma reservoir at a depth of <3 km more efficiently deforms the seafloor than tectonic earthquakes that typically occur at a depth of >10 km (Ward, 1982). Secondly, the combination of reverse slip along the ring fault and vertical motion of the horizontal crack localizes the coseismic uplift on a small area within the circular ring fault (Figures 6a and 9a–b). As such, trapdoor faulting can generate larger tsunamis than ordinary seismic faults of an equivalent fault size. However, at such shallow depths, the vertical motion of the horizontal crack and the two moment tensor elements, $M_{r\theta}$ and $M_{r\phi}$, of the ring fault are inefficient in radiating long-period seismic waves (Fukao et al., 2018; Sandanbata, Kanamori, et al., 2021), as shown earlier in Section 5. Additionally, the curved geometry of the ring fault also reduces long-period seismic amplitudes by the geometrical cancelation of the double-couple components (Ekström, 1994; Shuler, Ekström, et al., 2013; Sandanbata, Kanamori, et al., 2021).

6.3 Quasi-regular recurrence of submarine trapdoor faulting

We suggest that continuous magma supply below Sumisu caldera causes submarine trapdoor faulting almost every decade. By additional moment tensor analysis using long-period seismic data (Text S3), we estimate the *resolvable moment tensor* $\boldsymbol{M_{res}}$ for the four earthquakes, which was studied in Sandanbata, Kanamori, et al. (2021) to constrain the ring fault geometry. The resolvable moment tensors characterized by the null-axis direction and the ratio of the vertical-CLVD component (k_{CLVD}), which was introduced in Sandanbata, Kanamori et al. (2021) and is explained in Text S1, are similar for the 1996, 2006, and 2015 earthquakes (Figures 12a–c). These similarities indicate that, at the times of the earthquakes, trapdoor faulting occurred along almost the same ring fault segment of the source model for the 2015 earthquake (Figure

4a). This interpretation is supported by their similar tsunami waveforms recorded at tide gauges (Figures 1d–e and S1). The overall recurrence interval of ~10 yr may correspond to the time required to accumulate enough magma overpressure within the reservoir to rupture the ring fault (Cabaniss et al., 2020; Gregg et al., 2018). On the other hand, the resolvable moment tensor for the 2018 earthquake, which occurred only three years after the 2015 earthquake, contains a more dominant double-couple component (i.e., smaller k_{CLVD}) and has a smaller moment magnitude M_w (Figure 12d), suggesting that the trapdoor faulting in 2018 caused a rupture along a ring fault segment with a shorter arc length than those for the other events. This may explain the smaller tsunami associated with the 2018 earthquake (Figures 1d–e and S1). Some complexities linked to source geometries, frictional properties along the ring fault, or magma supply rate may cause variations in the size, the ring-fault length, and the recurrence interval of trapdoor faulting. For seismic waveform comparison, we show the results of moment tensor analyses for the four events in Figures S16–19.

The topography of Sumisu caldera also reflects the longer-term recurrence of trapdoor faulting. Our source model predicts that the submarine trapdoor faulting in 2015 uplifted the northeastern part of the caldera floor but caused little deformation in its southwestern part (Figure 12e). Along a SW–NE profile across the caldera (A–B in Figure 12e), coseismic vertical displacement with an offset of about 4 m correlates with the caldera floor topography, which slopes upward from the SW to NE with an altitude offset of ~150 m (Figure 12f). A similar correlation was found at Sierra Negra caldera (Amelung et al., 2000), where trapdoor faulting has occurred repeatedly due to continuous magma input. This suggests that magma supply has been continuous at Sumisu caldera, thereby causing submarine trapdoor faulting repeatedly and forming the slope of the caldera floor. Since an explosive submarine eruption in 1916 (Japan

Meteorological Agency, 2013), no clear evidence of eruptions has been found at Sumisu caldera and the relationship between trapdoor faulting and eruptions is still unclear.

6.4 Mechanisms of volcanic tsunami generation

Various mechanisms have been proposed to generate volcanic tsunamis: submarine explosions, pyroclastic flows, flank failures, caldera collapses, volcanic earthquakes accompanying eruptions, and interactions of ocean waves with atmospheric waves from volcanic explosions (Paris, 2015; Paris et al., 2014). The submarine trapdoor faulting mechanism identified in this study may be categorized as a volcanic earthquake mechanism, but is characterized by large-amplitude tsunamis without significant seismic radiation and by quasi-regular recurrence. This mechanism may also explain unusual tsunamis with similar characteristics generated near volcanic islands in the Kermadec arc, north of New Zealand (Gusman et al., 2020). These volcanic tsunamis due to submarine trapdoor faulting suggest that continuous monitoring of submarine calderas is necessary to reliably assess tsunami hazards.

7 Conclusions

By using remotely observed tsunami and long-period seismic data for the 2015 earthquake at Sumisu caldera, we constructed a fault-crack composite source model of submarine trapdoor faulting, which can quantitatively explain both datasets. The combined waveform analyses also allow us to constrain the magma reservoir depth and the ring fault geometry. Based on the model, we show that the atypical source properties, or large slip on a shallow and complex structure, contributed to meter-scale tsunami generation despite the

554 moderate seismic magnitude. The sub-decadal recurrence of trapdoor faulting with similar
555 tsunamis and seismic characters suggests that continuous magma supply into the submarine
556 caldera has been taking place. Further investigations of the submarine caldera using *in situ*
557 geophysical instruments, such as hydrophones, seismometers, pressure sensors, and ship-borne
558 surveys will be useful for understanding the volcanism, including the magma accumulation
559 process. This may lead to improved predictions of future submarine trapdoor faulting and/or
560 eruptions.

561

562 **Acknowledgments**

563 We thank Paul Segall and an anonymous reviewer for their constructive comments to improve
564 our manuscript. We thank Editor, Rachel Abercrombie, and Associate Editor, Lingling Ye, for
565 their valuable suggestions. We thank Aditya Gusman for providing the digitized tide gauge data.
566 We thank Dapeng Zaho for providing the velocity model used in our computation of seismic
567 waves. We thank Yoshio Fukao, Hiroko Sugioka, Aki Ito, and Hajime Shiobara for helping
568 obtain some of the tsunami data. This research was funded by JSPS KAKENHI (Grants
569 JP17J02919, JP20J01689, and JP19K04034) and JST J-RAPID (Grant JPMJJR1805). The travel
570 of Osamu Sandanbata to the California Institute of Technology was supported by the Overseas
571 Internship Program of the Earthquake Research Institute, The University of Tokyo.

572

573 **Open Research**

574 The earthquake data are from the Global CMT catalog (Ekström et al., 2012;
575 https://www.globalcmt.org/). Tide gauge data are available on request from the Japan

Meteorological Agency (https://www.jma.go.jp/jma/indexe.html) and Hydrographic and Oceanographic Department, Japan Coast Guard (https://www1.kaiho.mlit.go.jp/TIDE/gauge/index_eng.php) upon requests. Bathymetric data of M7000 Digital Bathymetric Chart and JTOPO30 are available from the Japan Hydrographic Association (https://www.jha.or.jp/shop/index.php?main_page=index) and GEBCO_2014 Grid is available from GEBCO Compilation Group (Weatherall et al., 2015; https://www.gebco.net/data_and_products/gridded_bathymetry_data/gebco_30_second_grid/). Ocean bottom pressure data of the array off Aogashima Island (Fukao et al., 2019) and the Deep Sea Floor Observatory off Muroto Cape (Momma et al., 1997) are available from the Japan Agency for Marine-Earth Science and Technology (http://p21.jamstec.go.jp/top/; under construction at the time of publication), DONET data are available from National Research Institute for Earth Science and Disaster Resilience (National Research Institute for Earth Science and Disaster Resilience, 2019a; https://www.seafloor.bosai.go.jp/), and DART data is available from National Oceanic and Atmospheric Administration (National Oceanic and Atmospheric Administration. 2005; https://nctr.pmel.noaa.gov/Dart/). F-net seismic data of F-net are available from the NIED (National Research Institute for Earth Science and Disaster Resilience, 2019b; https://www.fnet.bosai.go.jp/top.php?LANG=en), and Global Seismograph Network data are available through the IRIS Wilber 3 system (https://ds.iris.edu/wilber3/) or IRIS Web Services (https://service.iris.edu/), including the IU seismic network (GSN; Albuquerque, 1988). The source models presented in this paper are detailed in Data Set S1.

References

Aki, K., & Richards, P. G. (1980). *Quantitative seismology: theory and methods* (Vol. 842). Freeman San Francisco, CA.

Albuquerque Seismological Laboratory (ASL)/USGS. (1988). Global Seismograph Network (GSN – IRIS/USGS) [Data set]. International Federation of Digital Seismograph Networks. https://doi.org/10.7914/SN/IU.

Amelung, F., Jónsson, S., Zebker, H., & Segall, P. (2000). Widespread uplift and 'trapdoor' faulting on Galápagos volcanoes observed with radar interferometry. *Nature*, *407*(6807), 993–996. https://doi.org/10.1038/35039604.

Baba, T., Takahashi, N., Kaneda, Y., Ando, K., Matsuoka, D., & Kato, T. (2015). Parallel Implementation of Dispersive Tsunami Wave Modeling with a Nesting Algorithm for the 2011 Tohoku Tsunami. *Pure and Applied Geophysics*, *172*(12), 3455–3472. https://doi.org/10.1007/s00024-015-1049-2.

Bathke, H., Nikkhoo, M., Holohan, E. P., & Walter, T. R. (2015). Insights into the 3D architecture of an active caldera ring-fault at Tendürek volcano through modeling of geodetic data. *Earth and Planetary Science Letters*, *422*, 157–168. https://doi.org/10.1016/j.epsl.2015.03.041.

Cabaniss, H. E., Gregg, P. M., Nooner, S. L., & Chadwick, W. W., Jr. (2020). Triggering of eruptions at Axial Seamount, Juan de Fuca Ridge. *Scientific Reports*, *10*(1), 10219. https://doi.org/10.1038/s41598-020-67043-0.

Chadwick, W. W., Geist, D. J., Jónsson, S., Poland, M., Johnson, D. J., & Meertens, C. M. (2006). A volcano bursting at the seams: Inflation, faulting, and eruption at Sierra Negra volcano, Galápagos. *Geology*, *34*(12), 1025–1028. https://doi.org/10.1130/G22826A.1.

620 Chikasada, N. Y. (2019). Short-wavelength Tsunami Observation Using Deep Ocean Bottom
621 Pressure Gauges. In *The 29th International Ocean and Polar Engineering Conference*.
622 International Society of Offshore and Polar Engineers. Retrieved from
623 https://onepetro.org/conference-paper/ISOPE-I-19-707.
624 Cole, J. W., Milner, D. M., & Spinks, K. D. (2005). Calderas and caldera structures: a review.
625 *Earth-Science Reviews*, *69*(1), 1–26. https://doi.org/10.1016/j.earscirev.2004.06.004.
626 Contreras-Arratia, R., & Neuberg, J. W. (2019). Complex seismic sources in volcanic
627 environments: Radiation modelling and moment tensor inversions. *Journal of*
628 *Volcanology and Geothermal Research*, *381*, 262–272.
629 https://doi.org/10.1016/j.jvolgeores.2019.06.005.
630 Dahlen, F. A., & Tromp, J. (1998). *Theoretical Global Seismology*. Princeton University Press.
631 Duputel, Z., Rivera, L., Kanamori, H., & Hayes, G. (2012). W phase source inversion for
632 moderate to large earthquakes (1990–2010). *Geophysical Journal International*, *189*(2),
633 1125–1147. https://doi.org/10.1111/j.1365-246X.2012.05419.x.
634 Ekström, G. (1994). Anomalous earthquakes on volcano ring-fault structures. *Earth and*
635 *Planetary Science Letters*, *128*(3-4), 707–712. https://doi.org/10.1016/0012-
636 821x(94)90184-8.
637 Ekström, G., Nettles, M., & Dziewoński, A. M. (2012). The global CMT project 2004–2010:
638 Centroid-moment tensors for 13,017 earthquakes. *Physics of the Earth and Planetary*
639 *Interiors*, *200-201*, 1–9. https://doi.org/10.1016/j.pepi.2012.04.002.
640 Fukao, Y., Miyama, T., Tono, Y., Sugioka, H., Ito, A., Shiobara, H., et al. (2019). Detection of
641 ocean internal tide source oscillations on the slope of Aogashima island, japan. *Journal of*

642 *Geophysical Research, C: Oceans*, *124*(7), 4918–4933.
643 https://doi.org/10.1029/2019jc014997.
644 Fukao, Y., Sandanbata, O., Sugioka, H., Ito, A., Shiobara, H., Watada, S., & Satake, K. (2018).
645 Mechanism of the 2015 volcanic tsunami earthquake near Torishima, Japan. *Science*
646 *Advances*, *4*(4), eaao0219. https://doi.org/10.1126/sciadv.aao0219.
647 Galetto, F., Bagnardi, M., Acocella, V., & Hooper, A. (2019). Noneruptive unrest at the caldera
648 of Alcedo volcano (Galápagos islands) revealed by InSAR data and geodetic modeling.
649 *Journal of Geophysical Research, [Solid Earth]*, *124*(4), 3365–3381.
650 https://doi.org/10.1029/2018jb017103.
651 Gregg, P. M., Le Mével, H., Zhan, Y., Dufek, J., Geist, D., & Chadwick, W. W., Jr. (2018).
652 Stress triggering of the 2005 eruption of Sierra Negra volcano, Galápagos. *Geophysical*
653 *Research Letters*, *45*(24), 13288–13297. https://doi.org/10.1029/2018gl080393.
654 Grilli, S. T., Tappin, D. R., Carey, S., Watt, S. F. L., Ward, S. N., Grilli, A. R., et al. (2019).
655 Modelling of the tsunami from the December 22, 2018 lateral collapse of Anak Krakatau
656 volcano in the Sunda Straits, Indonesia. *Scientific Reports*, *9*(1), 11946.
657 https://doi.org/10.1038/s41598-019-48327-6.
658 Gusman, A. R., Kaneko, Y., Power, W., & Burbidge, D. (2020). Source process for two
659 enigmatic repeating vertical‐T CLVD tsunami earthquakes in the kermadec ridge.
660 *Geophysical Research Letters*, *47*(16). https://doi.org/10.1029/2020gl087805.
661 Hanks, T. C., & Kanamori, H. (1979). A moment magnitude scale. *Journal of Geophysical*
662 *Research*, *84*(B5), 2348. https://doi.org/10.1029/jb084ib05p02348.

663 Hayes, G. P., Rivera, L., & Kanamori, H. (2009). Source Inversion of the W-Phase: Real-time
664 Implementation and Extension to Low Magnitudes. *Seismological Research Letters*,
665 *80*(5), 817–822. https://doi.org/10.1785/gssrl.80.5.817.
666 Herrmann, R. B. (2013). Computer Programs in Seismology: An Evolving Tool for Instruction
667 and Research. *Seismological Research Letters*, *84*(6), 1081–1088.
668 https://doi.org/10.1785/0220110096.
669 Ho, T.-C., Satake, K., & Watada, S. (2017). Improved phase corrections for transoceanic tsunami
670 data in spatial and temporal source estimation: Application to the 2011 Tohoku
671 earthquake. *Journal of Geophysical Research, [Solid Earth]*, *122*(12), 10155–10175.
672 https://doi.org/10.1002/2017jb015070.
673 Hossen, M. J., Cummins, P. R., Dettmer, J., & Baba, T. (2015). Time reverse imaging for far-
674 field tsunami forecasting: 2011 Tohoku earthquake case study. *Geophysical Research*
675 *Letters*, *42*(22), 9906–9915. https://doi.org/10.1002/2015gl065868.
676 Hunt, J. E., Tappin, D. R., Watt, S. F. L., Susilohadi, S., Novellino, A., Ebmeier, S. K., et al.
677 (2021). Submarine landslide megablocks show half of Anak Krakatau island failed on
678 December 22nd, 2018. *Nature Communications*, *12*(1), 2827.
679 https://doi.org/10.1038/s41467-021-22610-5.
680 Japan Meteorological Agency. (2013). NATIONAL CATALOGUE OF THE ACTIVE
681 VOLCANOES IN JAPAN. Retrieved from
682 https://www.data.jma.go.jp/svd/vois/data/tokyo/STOCK/souran_eng/menu.htm.
683 Jónsson, S. (2009). Stress interaction between magma accumulation and trapdoor faulting on
684 Sierra Negra volcano, Galápagos. *Tectonophysics*, *471*(1), 36–44.
685 https://doi.org/10.1016/j.tecto.2008.08.005.

686 Kajiura, K. (1963). The Leading Wave of a Tsunami. *Bulletin of the Earthquake Research*
687 *Institute, University of Tokyo*, *41*(3), 535–571. Retrieved from
688 https://ci.nii.ac.jp/naid/120000866529/.
689 Kanamori, H. (1972). Mechanism of tsunami earthquakes. *Physics of the Earth and Planetary*
690 *Interiors*, *6*(5), 346–359. https://doi.org/10.1016/0031-9201(72)90058-1.
691 Kanamori, H. (1977). The energy release in great earthquakes. *Journal of Geophysical Research*,
692 *82*(20), 2981–2987. https://doi.org/10.1029/jb082i020p02981.
693 Kanamori, H., & Rivera, L. (2008). Source inversion of Wphase: speeding up seismic tsunami
694 warning. *Geophysical Journal International*, *175*(1), 222–238.
695 https://doi.org/10.1111/j.1365-246X.2008.03887.x.
696 Kanamori, H., Ekström, G., Dziewonski, A., Barker, J. S., & Sipkin, S. A. (1993). Seismic
697 radiation by magma injection: An anomalous seismic event near Tori Shima, Japan.
698 *Journal of Geophysical Research*, *98*(B4), 6511–6522.
699 https://doi.org/10.1029/92jb02867.
700 Kawakatsu, H., & Yamamoto, M. (2015). 4.15 - Volcano Seismology. In G. Schubert (Ed.),
701 *Treatise on Geophysics (Second Edition)* (pp. 389–419). Oxford: Elsevier.
702 https://doi.org/10.1016/B978-0-444-53802-4.00081-6.
703 Kodaira, S., Sato, T., Takahashi, N., Ito, A., Tamura, Y., Tatsumi, Y., & Kaneda, Y. (2007).
704 Seismological evidence for variable growth of crust along the Izu intraoceanic arc.
705 *Journal of Geophysical Research*, *112*(B5). https://doi.org/10.1029/2006jb004593.
706 Liu, Y.-K., Ruch, J., Vasyura-Bathke, H., & Jónsson, S. (2019). Influence of ring faulting in
707 localizing surface deformation at subsiding calderas. *Earth and Planetary Science*
708 *Letters*, *526*, 115784. https://doi.org/10.1016/j.epsl.2019.115784.

709 Momma, H., Fujiwara, N., Kawaguchi, K., Iwase, R., Suzuki, S., & Kinoshita, H. (1997).
710 Monitoring system for submarine earthquakes and deep sea environment. In *Oceans '97.*
711 *MTS/IEEE Conference Proceedings* (Vol. 2, pp. 1453–1459 vol.2).
712 https://doi.org/10.1109/OCEANS.1997.624211.
713 National Oceanic and Atmospheric Administration. (2005). Deep-ocean assessment and
714 reporting of tsunamis (DART) [Data set]. National Geophysical Data Center, NOAA.
715 https://doi.org/10.7289/V5F18WNS.
716 National Research Institute for Earth Science and Disaster Resilience. (2019a). NIED DONET
717 [Data set]. National Research Institute for Earth Science and Disaster Resilience.
718 https://doi.org/10.17598/NIED.0008.
719 National Research Institute for Earth Science and Disaster Resilience. (2019b). NIED F-net
720 [Data set]. National Research Institute for Earth Science and Disaster Resilience.
721 https://doi.org/10.17598/NIED.0005.
722 Nikkhoo, M., & Walter, T. R. (2015). Triangular dislocation: an analytical, artefact-free solution.
723 *Geophysical Journal International*, *201*(2), 1119–1141.
724 https://doi.org/10.1093/gji/ggv035
725 Paris, R. (2015). Source mechanisms of volcanic tsunamis. *Philosophical Transactions. Series A,*
726 *Mathematical, Physical, and Engineering Sciences*, *373*(2053).
727 https://doi.org/10.1098/rsta.2014.0380.
728 Paris, R., Switzer, A. D., Belousova, M., Belousov, A., Ontowirjo, B., Whelley, P. L., &
729 Ulvrova, M. (2014). Volcanic tsunami: a review of source mechanisms, past events and
730 hazards in Southeast Asia (Indonesia, Philippines, Papua New Guinea). *Natural Hazards*,
731 *70*(1), 447–470. https://doi.org/10.1007/s11069-013-0822-8.

732 Peregrine, D. H. (1972). Equations for Water Waves and the Approximation behind Them. In R.
733 E. Meyer (Ed.), *Waves on Beaches and Resulting Sediment Transport* (pp. 95–121).
734 Academic Press. https://doi.org/10.1016/B978-0-12-493250-0.50007-2.
735 Persson, P.-O., & Strang, G. (2004). A Simple Mesh Generator in MATLAB. *SIAM Review.*
736 *Society for Industrial and Applied Mathematics*, *46*(2), 329–345.
737 https://doi.org/10.1137/s0036144503429121.
738 Roche, O., Druitt, T. H., & Merle, O. (2000). Experimental study of caldera formation. *Journal*
739 *of Geophysical Research*, *105*(B1), 395–416. https://doi.org/10.1029/1999jb900298.
740 Saito, T., & Furumura, T. (2009). Three-dimensional tsunami generation simulation due to sea-
741 bottom deformation and its interpretation based on the linear theory. *Geophysical Journal*
742 *International*, *178*(2), 877–888. https://doi.org/10.1111/j.1365-246X.2009.04206.x.
743 Sandanbata, O., Kanamori, H., Rivera, L., Zhan, Z., Watada, S., & Satake, K. (2021). Moment
744 tensors of ring-faulting at active volcanoes: Insights into vertical-CLVD earthquakes at
745 the Sierra Negra caldera, Galápagos islands. *Journal of Geophysical Research, [Solid*
746 *Earth]*, *126*(6), e2021JB021693. https://doi.org/10.1029/2021jb021693.
747 Sandanbata, O., Watada, S., Ho, T.-C., & Satake, K. (2021). Phase delay of short-period
748 tsunamis in the density-stratified compressible ocean over the elastic Earth. *Geophysical*
749 *Journal International*, *226*(3), 1975–1985. https://doi.org/10.1093/gji/ggab192.
750 Satake, K. (2015). 4.19 - Tsunamis. In G. Schubert (Ed.), *Treatise on Geophysics (Second*
751 *Edition)* (pp. 477–504). Oxford: Elsevier. https://doi.org/10.1016/B978-0-444-53802-
752 4.00086-5.

753 Satake, K., & Kanamori, H. (1991). Abnormal tsunamis caused by the June 13, 1984, Torishima,
754 Japan, earthquake. *Journal of Geophysical Research*, *96*(B12), 19933–19939.
755 https://doi.org/10.1029/91jb01903.
756 Shukuno, H., Tamura, Y., Tani, K., Chang, Q., Suzuki, T., & Fiske, R. S. (2006). Origin of
757 silicic magmas and the compositional gap at Sumisu submarine caldera, Izu–Bonin arc,
758 Japan. *Journal of Volcanology and Geothermal Research*, *156*(3), 187–216.
759 https://doi.org/10.1016/j.jvolgeores.2006.03.018.
760 Shuler, A., Nettles, M., & Ekström, G. (2013). Global observation of vertical-CLVD earthquakes
761 at active volcanoes. *Journal of Geophysical Research, [Solid Earth]*, *118*(1), 138–164.
762 https://doi.org/10.1029/2012jb009721.
763 Shuler, A., Ekström, G., & Nettles, M. (2013). Physical mechanisms for vertical-CLVD
764 earthquakes at active volcanoes. *Journal of Geophysical Research, [Solid Earth]*, *118*(4),
765 1569–1586. https://doi.org/10.1002/jgrb.50131.
766 Silver, P. G., & Jordan, T. H. (1982). Optimal estimation of scalar seismic moment. *Geophysical*
767 *Journal International*, *70*(3), 755–787. https://doi.org/10.1111/j.1365-
768 246X.1982.tb05982.x.
769 Tani, K., Fiske, R. S., Tamura, Y., Kido, Y., Naka, J., Shukuno, H., & Takeuchi, R. (2008).
770 Sumisu volcano, Izu-Bonin arc, Japan: site of a silicic caldera-forming eruption from a
771 small open-ocean island. *Bulletin of Volcanology*, *70*(5), 547–562.
772 https://doi.org/10.1007/s00445-007-0153-2.
773 Tappin, D. R., Matsumoto, T., Watts, P., Satake, K., McMurtry, G. M., Matsuyama, M., et al.
774 (1999). Sediment slump likely caused 1998 Papua New Guinea tsunami. *Eos*, *80*(30),
775 329. https://doi.org/10.1029/99eo00241.

776 Walter, T. R., Haghshenas Haghighi, M., Schneider, F. M., Coppola, D., Motagh, M., Saul, J., et
777 al. (2019). Complex hazard cascade culminating in the Anak Krakatau sector collapse.
778 *Nature Communications*, *10*(1), 4339. https://doi.org/10.1038/s41467-019-12284-5.
779 Ward, S. N. (1982). On tsunami nucleation II. An instantaneous modulated line source. *Physics*
780 *of the Earth and Planetary Interiors*, *27*, 273–285.
781 Ward, S. N. (2001). Landslide tsunami. *Journal of Geophysical Research*, *106*(B6), 11201–
782 11215. https://doi.org/10.1029/2000jb900450.
783 Weatherall, P., Marks, K. M., & Jakobsson, M. (2015). A new digital bathymetric model of the
784 world's oceans. *Earth and Space*. https://doi.org/10.1002/2015EA000107.
785 Wells, D. L., & Coppersmith, K. J. (1994). New Empirical Relationships among Magnitude,
786 Rupture Length, Rupture Width, Rupture Area, and Surface Displacement. *Bulletin of the*
787 *Seismological Society of America*, *84*(4), 974–1002.
788 https://doi.org/10.1785/BSSA0840040974.
789 Yun, S.-H. (2007). *A mechanical model of the large-deformation 2005 Sierra Negra volcanic*
790 *eruption derived from InSAR measurements* (Ph.D. Desertation). Stanford University.
791 Retrieved from https://web.stanford.edu/group/radar/people/Yun_thesis_small.pdf
792 Zheng, Y., Blackstone, L., & Segall, P. (2022). Constraints on absolute magma chamber volume
793 from geodetic measurements of trapdoor faulting at Sierra Negra volcano, Galapagos.
794 *Geophysical Research Letters*, *49*(5). https://doi.org/10.1029/2021gl095683.
795
796

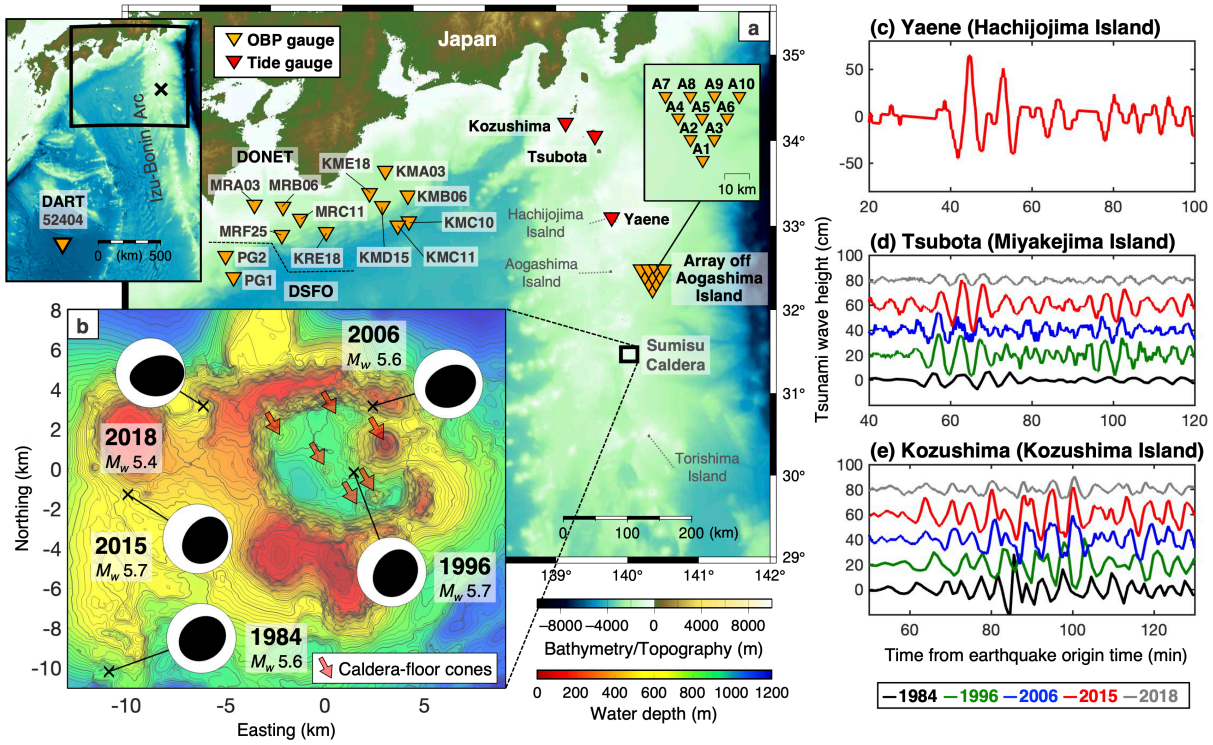

797

798 **Figure 1.** Anomalous tsunamis due to volcanic earthquakes at Sumisu caldera. (**a**) Map showing
799 the locations of Sumisu caldera, ocean bottom pressure gauges (orange triangles), and
800 representative tide gauges (red triangles). (**b**) Repeating earthquakes near Sumisu caldera
801 reported by the GCMT catalog (Ekström et al., 2012). The focal mechanisms are shown by
802 projection of the lower focal hemisphere. Arrows point to cones on the caldera floor, some of
803 which were identified as lava domes (Tani et al., 2008). (**c**) Tsunami waveform from the 2015
804 earthquake recorded by the tide gauge at Yaene (Hachijojima Island). (**d–e**) Tsunami waveforms
805 at Tsubota (Miyakejima Island) and Kozushima (Kozushima Island) from the repeating
806 earthquakes. Baselines for different events are shifted by multiples of 20 cm. Tsunami
807 waveforms at other tide gauge stations are shown in Figure S1.

808

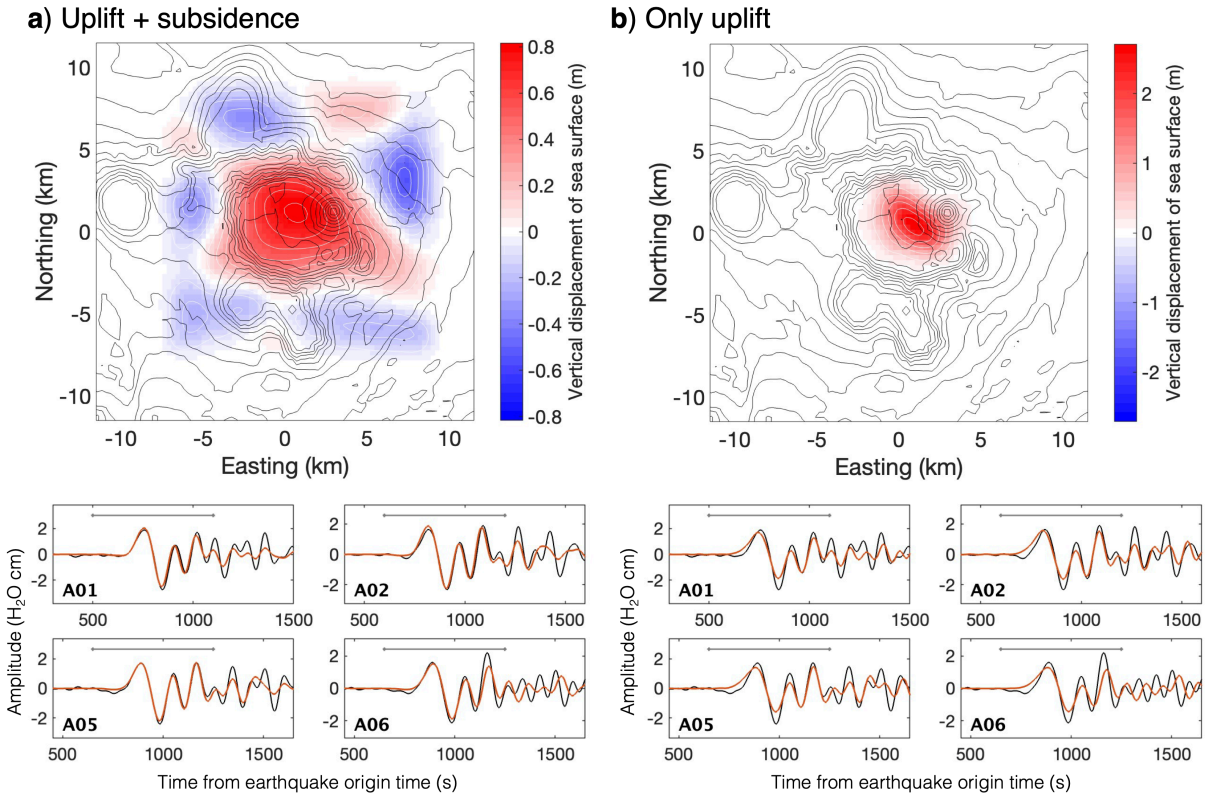

Figure 2. Preliminary initial sea-surface displacement models. Models with (**a**) both uplift and subsidence and (**b**) only uplift. (Top panel) Red and blue colors represent uplift and subsidence, respectively. Bathymetric contours at 100 m intervals. (Bottom panels) Comparison of the observed (black) and synthetic (red) tsunami waveforms at representative ocean bottom pressure gauges. The gray line represents the time interval used for the inversion.

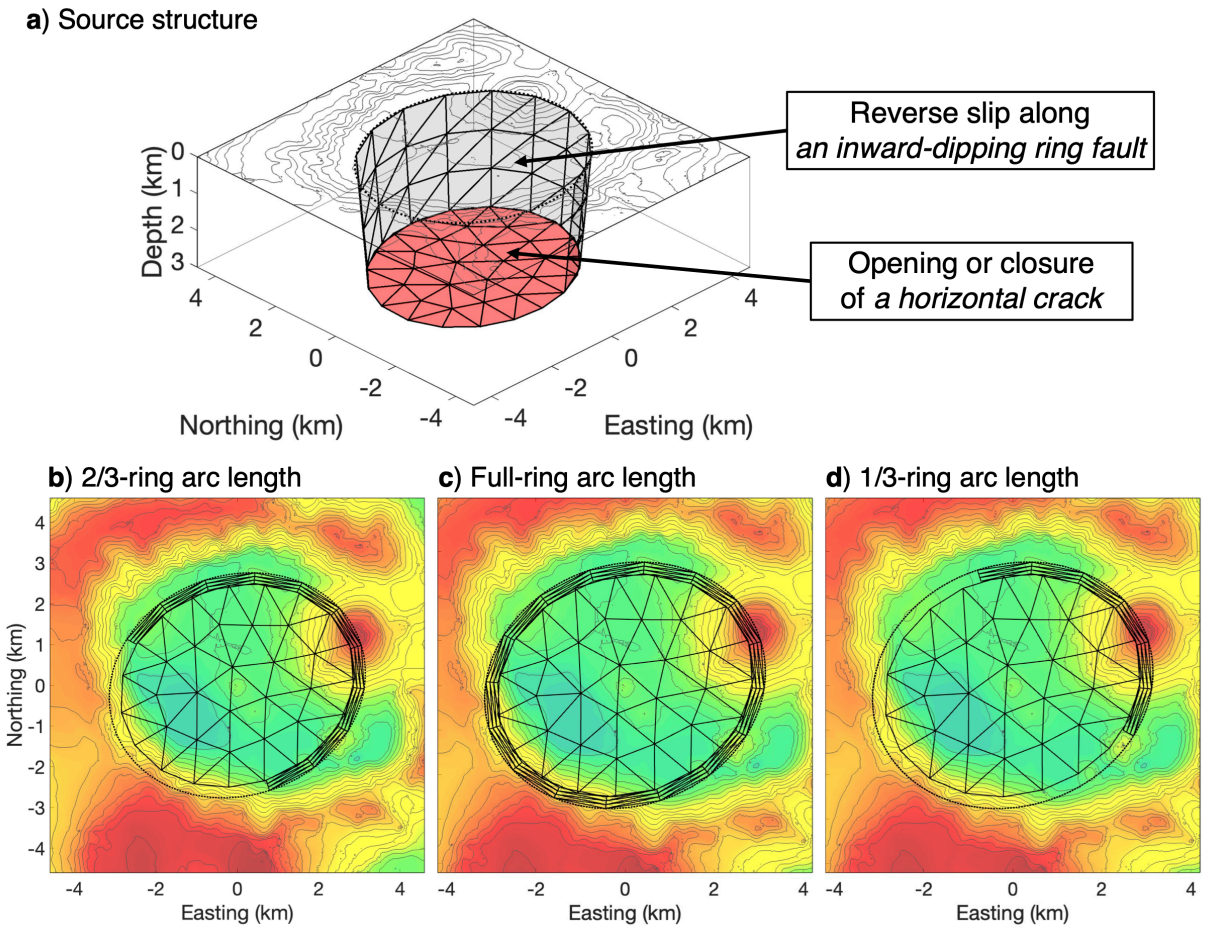

816

817 **Figure 3.** Fault-crack composite system assumed for the source modeling. (**a**) Example of the
818 source structure assumed in this study. (**b**–**d**) Three cases of the ring-fault arc length assumed in
819 the source modeling: (**b**) 2/3 ring, (**c**) full ring, and (**d**) 1/3 ring arc lengths.

820

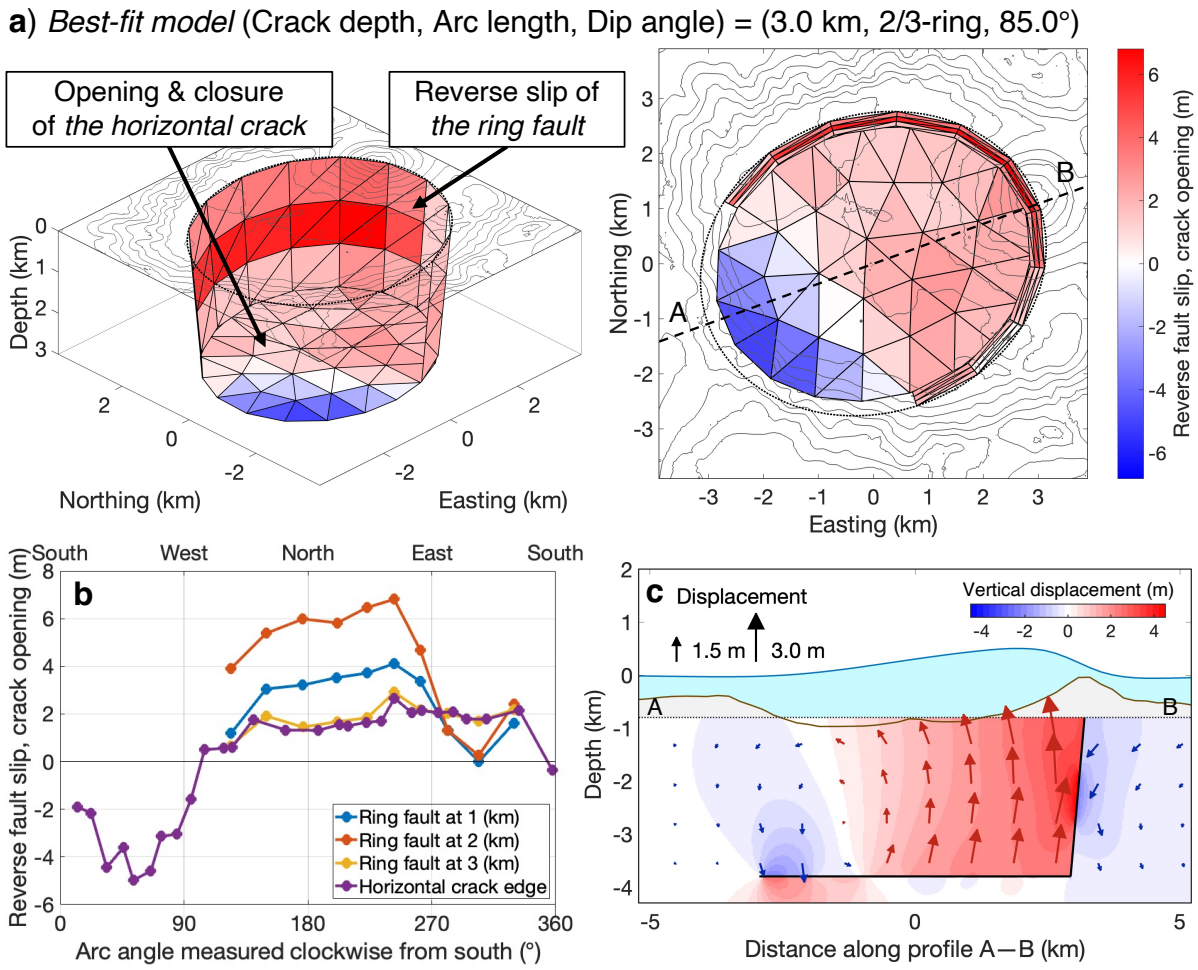

821

822 **Figure 4.** Best-fit source model for the 2015 earthquake. (**a**) Motions (dislocations) of the fault-
823 crack composite system viewed from the southwest (left panel) and above (right panel). The
824 horizontal crack is at a depth of 3 km, and the ring fault along two-thirds of the arc of the caldera
825 rim has a uniform dip angle of 85°. The red color on the ring fault represents reverse slip. Red
826 and blue colors on the horizontal crack represent vertical opening and closure, respectively. (**b**)
827 Amounts of reverse slip at sub-faults of the ring fault and opening or closing of sub-cracks on the
828 horizontal crack edge. The arc angle shown in the horizontal axis is measured clockwise from
829 south (black dot in the right panel of **a**). Circles in **b** are plotted at arc angles of centroids of the
830 sub-faults and sub-cracks. Note that the ring fault displacement at the bottom (3 km) is in

831 approximate agreement with that of the adjacent crack, because of the kinematic condition
832 (Equation 4). (**c**) Displacement of the caldera computed with the model along the A–B profile
833 shown in **a** (right panel). The red and blue colors indicate upward and downward displacements,
834 respectively. We assume that the bathymetry is flat for the computation. Note that the seafloor
835 and sea-surface displacements are exaggerated.
836

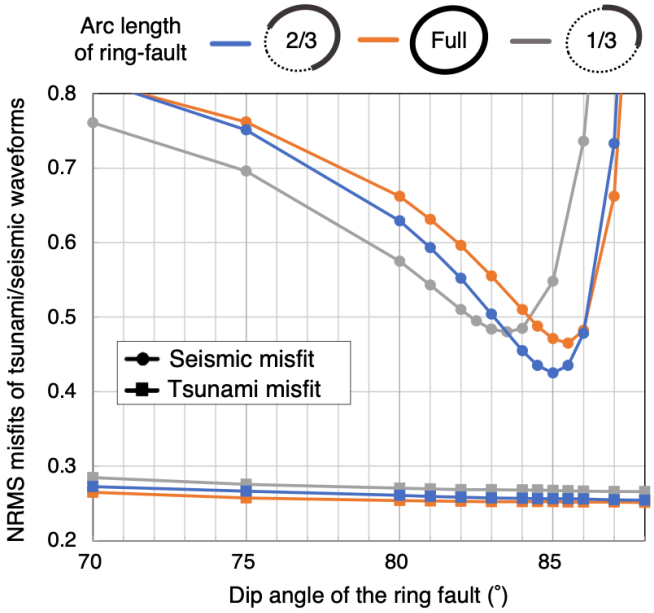

837

838 **Figure 5.** Comparison of the tsunami and seismic waveform misfits (Equations 8 and 11,
839 respectively) for source models with different ring-fault dip angles and arc lengths. All the
840 models shown here have the horizontal crack at a depth of 3 km.

841

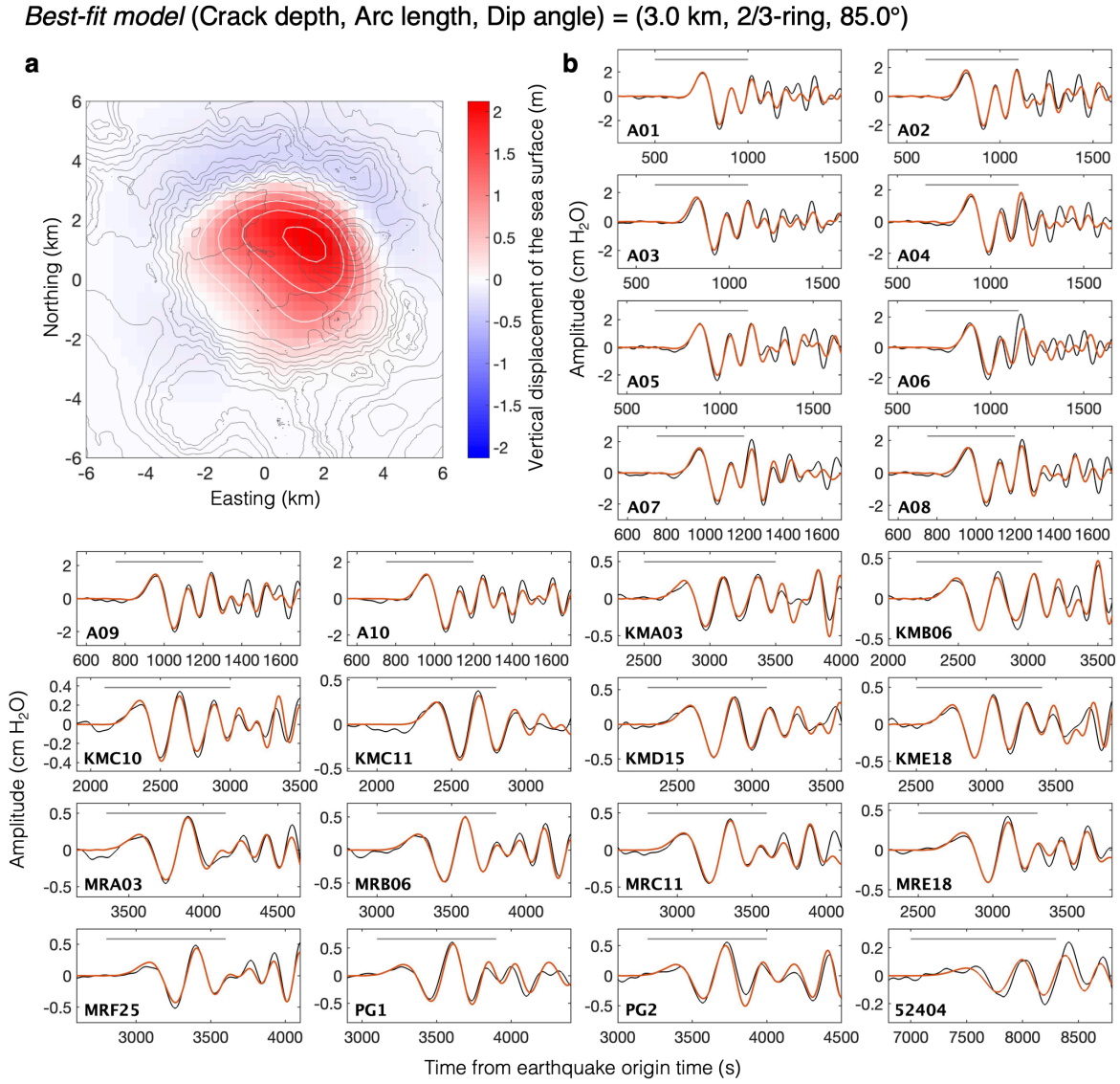

Figure 6. Tsunami waveforms from the best-fit source model (Figure 4a). (**a**) Vertical displacement of sea surface caused by the model. Red and blue colors represent uplift and subsidence, respectively, with white contour lines plotted every 0.5 m. Note that the color scale in this figure is different from that in Figure 2a. (**b**) Comparison of the observed (black) and synthetic (red) tsunami waveforms from the model at the ocean bottom pressure gauges. The gray line represents the time interval used for the inversion.

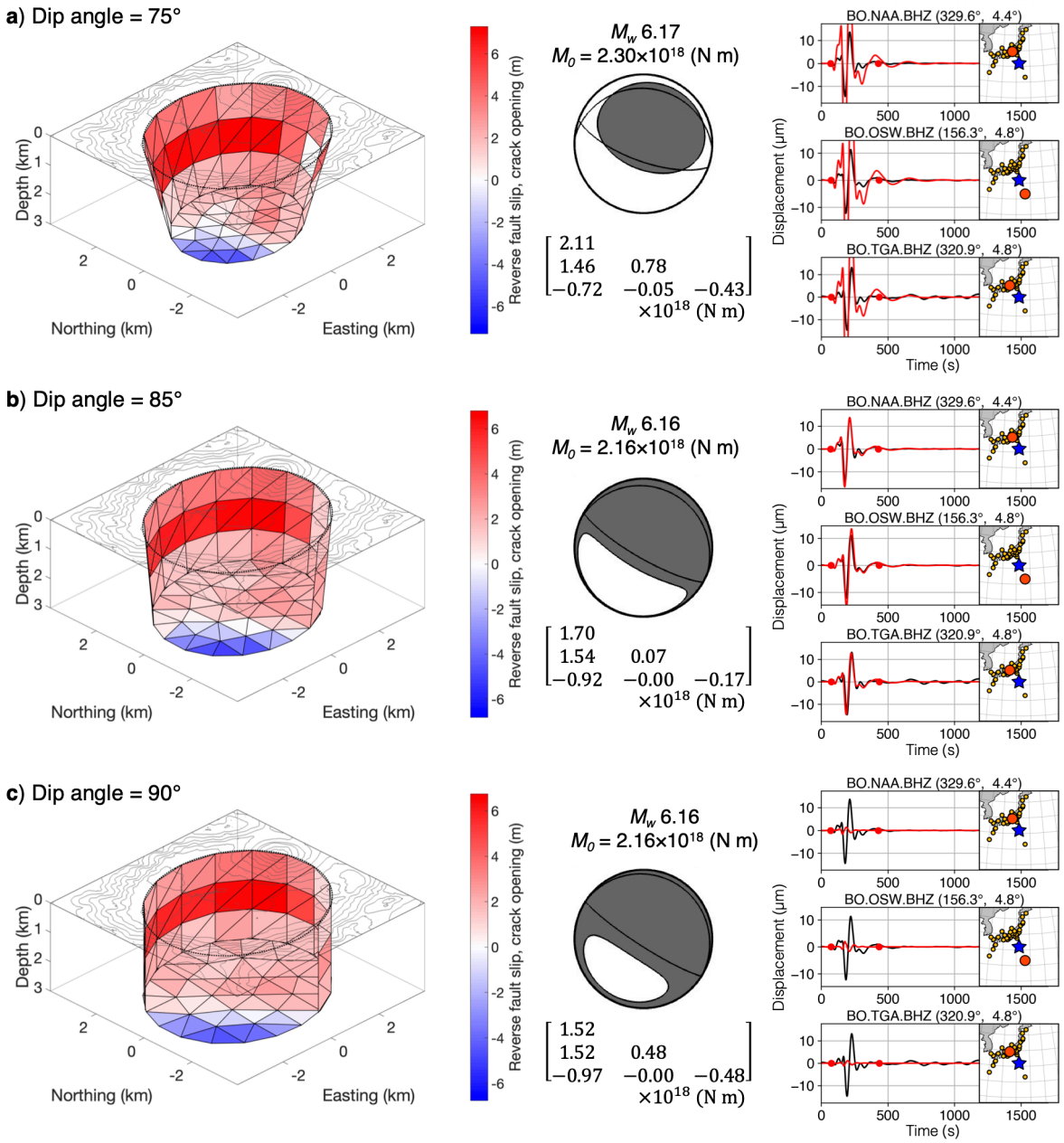

850

851 **Figure 7.** Long-period seismic data analyses from source models with the ring-fault dip angles
852 of (**a**) 75°, (**b**) 85°, and (**c**) 90°. (Left) Motions of the fault-crack composite system inverted from
853 the tsunami data. (Middle) Moment tensors of the model. The focal mechanisms are shown as
854 projections of the lower focal hemisphere, and the orientation of the best double-couple solution
855 is shown as thin lines. (Right) Comparison of the observed (black) and synthetic (red)

856 seismograms (period = 60–250 s) at representative stations. In each inset figure, a large red circle
857 and blue star represent the station and earthquake centroid, respectively. The network name,
858 station name, record component, station azimuth, and epicentral distance are given on the top of
859 each panel. Note that the amplitudes of the synthetic waveforms decrease as the ring-fault dip
860 angle increases.
861

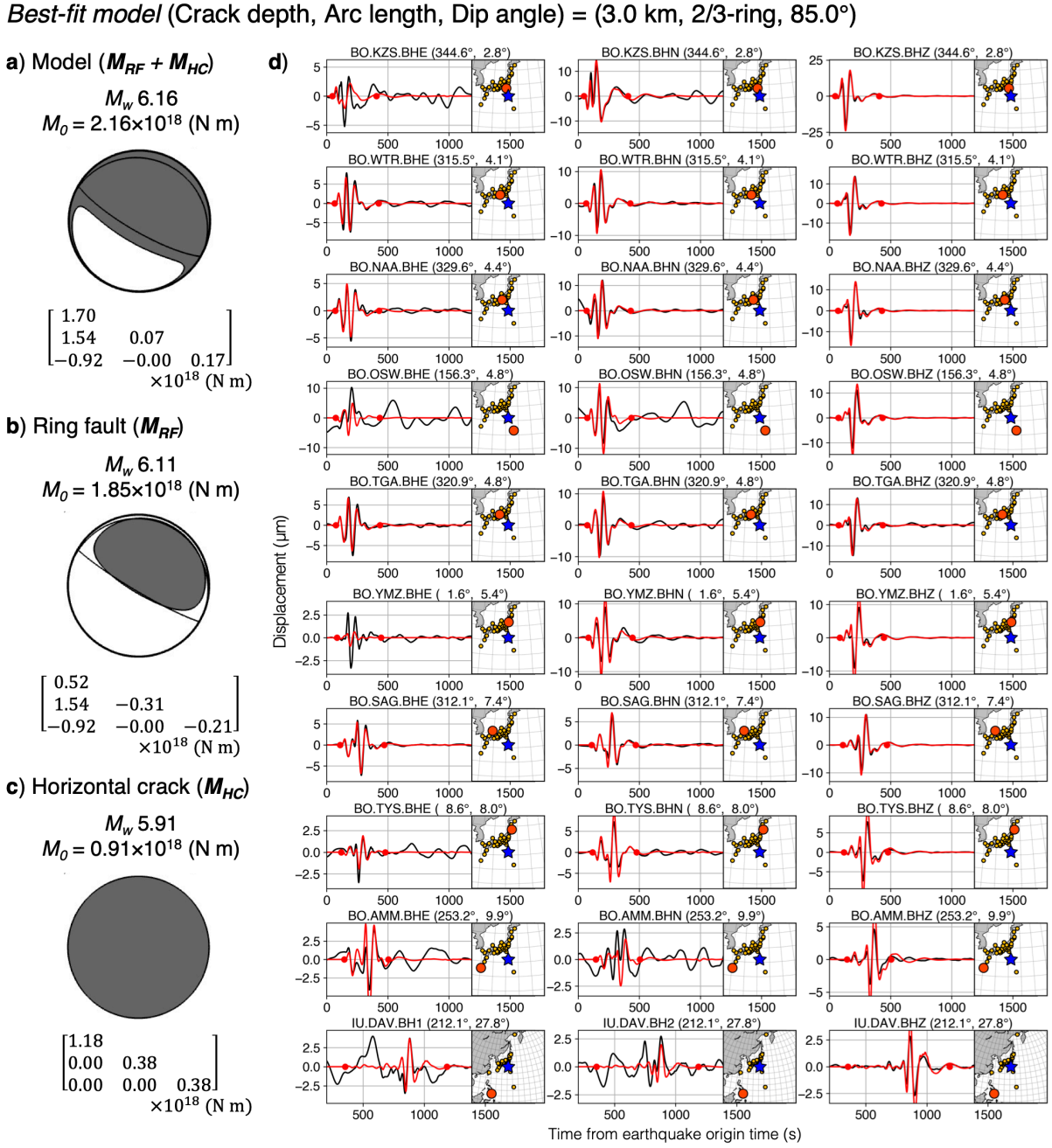

Figure 8. Long-period seismic data analyses from the best-fit source model (Figure 4a). (**a**) Moment tensors of the model. (**b**–**c**) Partial moment tensors of (**b**) the ring fault and (**c**) the horizontal crack. The focal mechanisms are shown as projections of the lower focal hemisphere, and the orientation of the best double-couple solution is shown as thin lines. (**d**) Comparison of

867 the observed (black) and synthetic (red) seismograms (period = 60–250 s), computed with the
868 moment tensor shown in **a** at representative stations. The data interval used to calculate the
869 waveform misfit is delimited by the red dots. See the caption for the right panel of Figure 7.
870

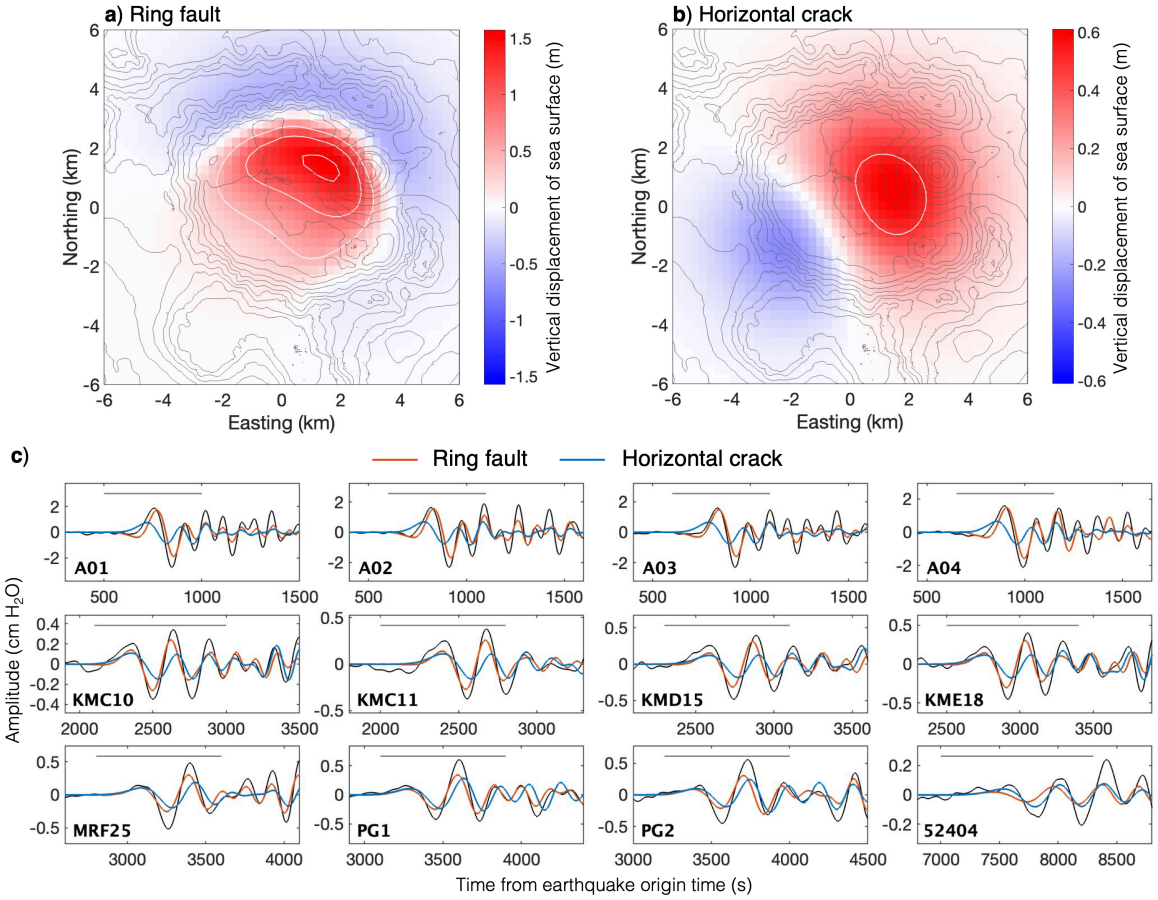

871

872 **Figure 9.** Partial contributions of the ring fault and the horizontal crack of the best-fit source
873 model (Figure 4a) to the tsunami waveforms. (**a–b**) Vertical sea-surface displacements caused by
874 (**a**) the ring fault and (**b**) the horizontal crack. Red and blue colors represent uplift and
875 subsidence, respectively, with white contour lines plotted every 0.5 m. (**c**) Comparison of the
876 synthetic tsunami waveforms from the ring fault (red) and the horizontal crack (blue), with the
877 observed (black) waveforms at representative OBP gauges. The gray line represents the time
878 interval used for the inversion.

879

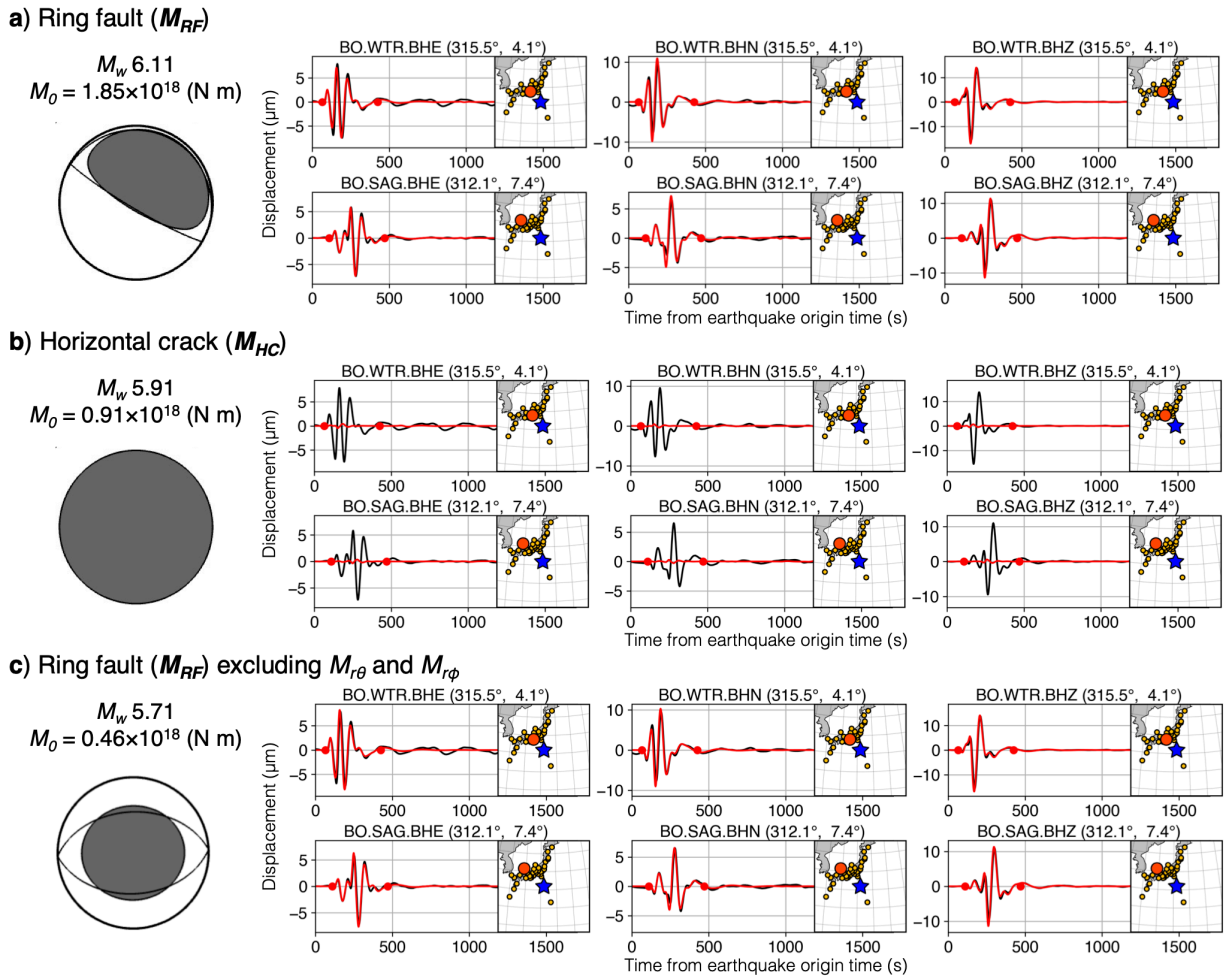

Figure 10. Contributions of the best-fit source model (Figure 4a) to the long-period seismic waves. Synthetic seismograms (red curves) from the moment tensors of (**a**) the ring fault $\boldsymbol{M_{RF}}$, (**b**) and horizontal crack $\boldsymbol{M_{HC}}$, and (**c**) the ring fault, but excluding the two elements $M_{r\theta}$ and $M_{r\phi}$ (i.e., M_{rr}, $M_{\theta\theta}$, $M_{\phi\phi}$, and $M_{\theta\phi}$ of $\boldsymbol{M_{RF}}$). Note that the synthetic seismic waveforms from the horizontal crack (**b**) are much smaller than those from the ring fault (**a**), and that the waveforms from the ring fault do not change although $M_{r\theta}$ and $M_{r\phi}$ are removed (compare the synthetic waveforms in **a** and **c**).

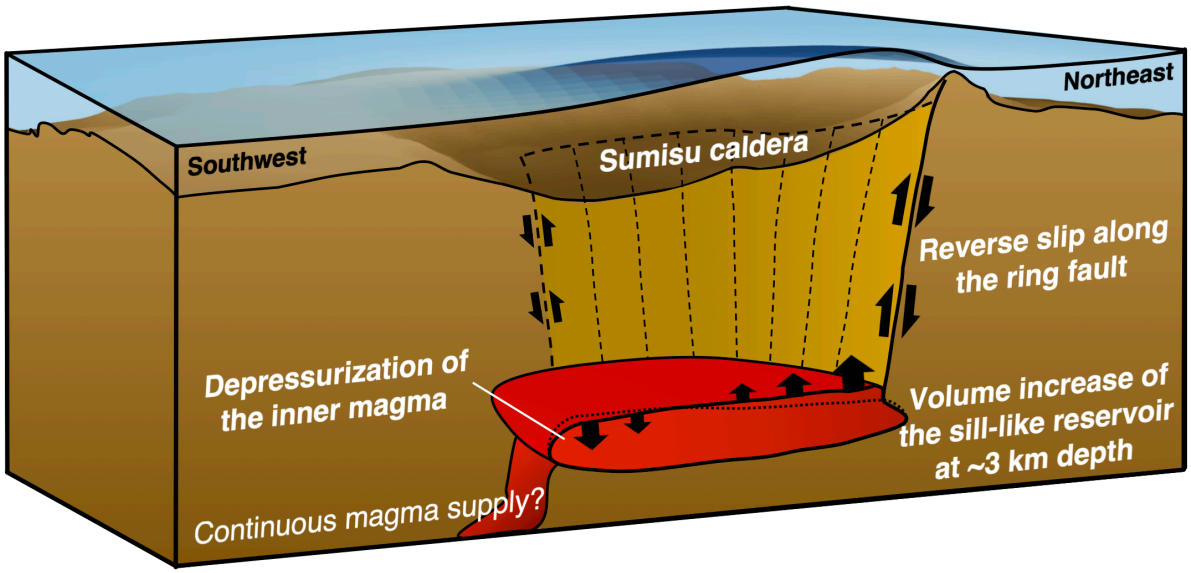

Figure 11. Schematic illustration of submarine trapdoor faulting mechanism at Sumisu caldera (not to scale). Reverse slip occurs along the ring fault, the sill-like reservoir opens vertically on the northeastern side of the caldera and consequent depressurization of the inner magma causes the downward motion of the upper wall of the southwestern part of the magma reservoir.

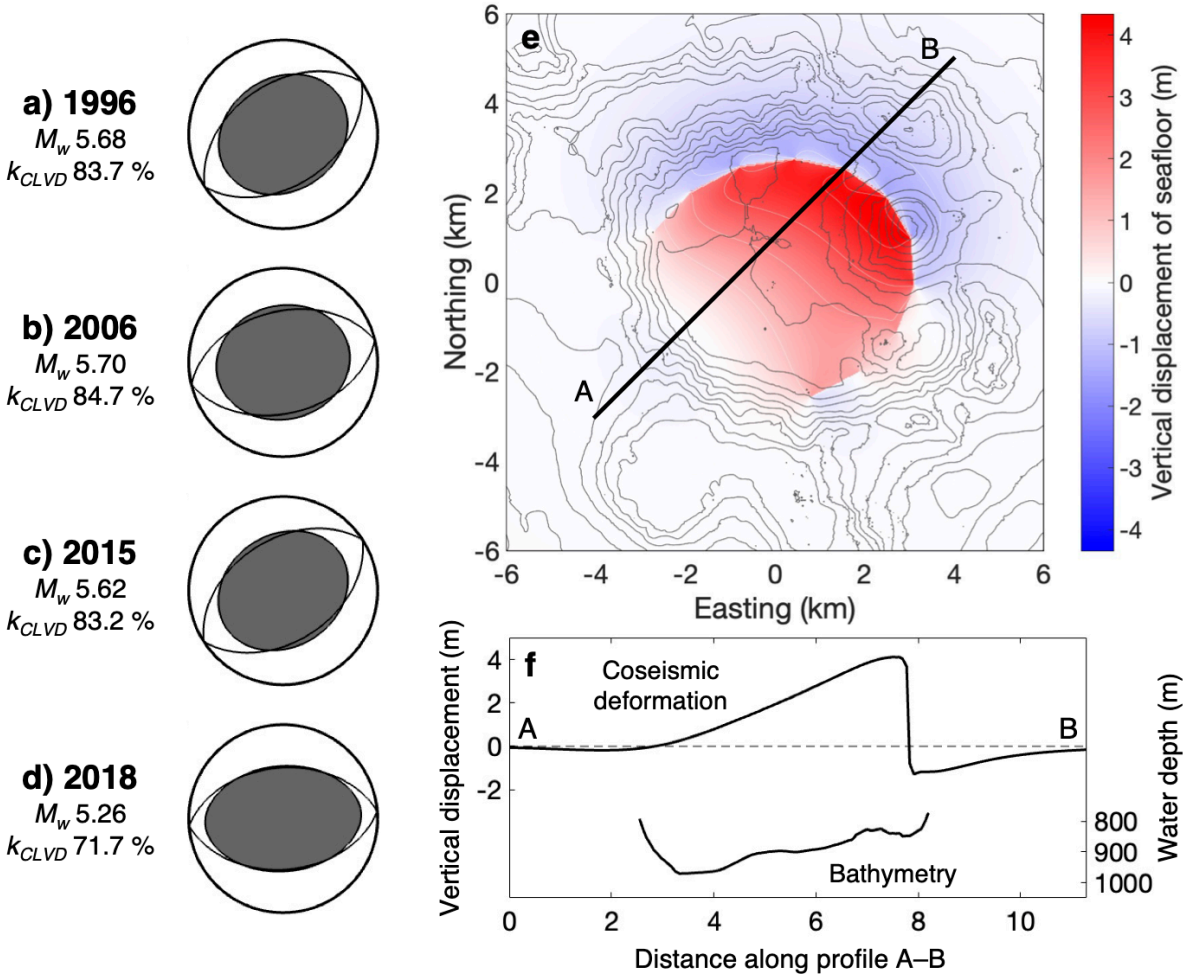

Figure 12. Recurrence of trapdoor faulting at Sumisu caldera. (**a**–**d**) Resolvable moment tensors $\boldsymbol{M}_{res}$ for the earthquakes in (**a**) 1996, (**b**) 2006, (**c**) 2015, and (**d**) 2018 estimated by our moment tensor analysis. The orientation of the best double-couple solution is shown by thin curves. M_w and k_{CLVD} indicate the moment magnitude of $\boldsymbol{M}_{res}$ and the dominancy of the vertical-CLVD component in $\boldsymbol{M}_{res}$, respectively. (**e**) Vertical seafloor displacement computed with the best-fit source model for the 2015 earthquake (Figure 4a). (**f**) Profiles of the vertical seafloor displacement and the topography along A–B shown in **e**.